The Effect of Asymmetric Fluid Flow Distribution on Flow Boiling in a Microchannel Heat Sink - an Experimental Investigation

Ritunesh Kumar[1]*,Gurjeet Singh[1], Dariusz Mikielewicz[2]

[1] Mechanical Engineering Department, Indian Institute of Technology Indore, Khandwa Road, Simrol,

India-453552

[2] Gdansk University of Technology, Faculty of Mechanical Engineering and Shipbuilding,

ul. Narutowicza 11/12, 80-233 Gdansk, Poland

[*] Corresponding author. Tel.: (+91) 7324 240734

Fax: +91 7324 240761

Email: ritunesh@iiti.ac.in

ABSTRACT

Flow boiling in microchannels is emerging as an exclusive cooling solution for miniaturized high-power electronic devices alongside having other high heat flux applications. Size miniaturization at microscale strangely increases heat transfer performance as well as flow boiling instabilities. Many flow boiling instabilities are interrelated and result from imperfect hydrodynamic conditions. One of such problems is flow maldistribution among parallel channels of a microchannel heat sink. Very limited studies have dedicatedly investigated the negative effects of flow maldistribution on the boiling process in microchannels. A microchannel heat sink with twenty-five rectangular microchannels (width × height × length = 0.45 × 0.725 × 25 mm) made on a copper block base of 25 × 25 × 85 mm using wire electrical discharge machining under an I-type flow configuration is investigated for that purpose. Flow boiling patterns of central and side microchannels as well as the temperature profile of central and side microchannels are recorded. The boiling process always incepts in side microchannels and rapidly converts into a periodic flow reversal up to the inlet manifold, whereas weak, stable, bubbly flow and single-phase liquid flow are observed in the neighboring and central microchannels, respectively. Furthermore, with the increase of heat flux, flow boiling intensity increases and more parallel microchannels start experiencing rapid bubble growth; consequently, the intensity of flow reversal in side channels also increases. At high heat fluxes, the vapor backflow of side microchannels reaches the central microchannel and blocks the flow through it, named mirage flow confinement. Boiling in the central channel aggravates under the influence of the mirage flow reversal processes. Temperature non-uniformity across the microchannel heat sink increases with the increase of heat flux and mass flux caused by the early appearance of a partial dry-out of side channels and the escalation of the flow distribution asymmetry,, whereas, better temperature distribution is observed at higher inlet fluid temperatures.

Keywords: Microchannel heat sink; flow maldistribution; flow boiling; flow visualization; instabilities;

1. Introduction

Continuous miniaturization of the metal-oxide-semiconductor field-effect-transistor's (MOSFET) size (~10 μm in 1971 to ~7 nm in 2019) has increased the computing power of modern-day microprocessors immensely in the last five decades [1]. This transformation has maximized

their power consumption from a few Watts to 250 W [2]. High power consumption means enormous heat generation which may cause thermal damage in the microprocessor, if it is not dissipated effectively from its tiny base. Thermal management has emerged as an equally important issue which may severly impede the advancement of desktop PCs and Laptops. Microchannel heat sinks are emerging as an exclusive solution to the abovementioned problem, as well as other critical issues [3-7], due to very high heat transfer rates. Other key attributes of microchannel heat sinks (MCHSs) are: low surface temperature, very low coolant inventory requirement and extremely compact design. Both, single and two-phase heat transfer have received considerable research attention targeting moderate and high heat flux applications [8]. In fact, two-phase heat transfer received more attention due to the inherent addition of heat transfer caused by the latent heat of fluid vaporization along with sensible heat transfer. Still, the main focus of the research has remained on understanding the early vapor locking of channels at microscale, which introduces many exclusive conceptual differences in boiling between macro and micro scale. Various transition criteria have been proposed to differentiate between the above. Kew and Cornwell [9] proposed Confinement number (Co) to distinguish between macro scale and micro scale. They suggested the threshold limit of $Co = 0.5$ for the identification of micro scale characteristics ($Co > 0.5$) associated with the boiling process. Ong and Thome [10] presented an improved confinement number range ($Co > 1$) for the microscale channel. Harirchian and Garimella [11] proposed a convective confinement number ($Bd^{0.5}Re < 160$) as limiting criteria to determine microscale channels, the newly defined number accounted the influence of mass flux on the physical confinement of a channel apart from thermo-physical properties and dimensions of the channel. Several researchers advocated transition criteria based on physical dimensions of the channel [12]. Furthermore, various dedicated, experimental and theoretical studies have been carried out in order to understand the flow boiling phenomenon in microchannels [13-20].

Flow boiling at micro level offers salient benefits, such as much higher convective heat transfer coefficient and uniform surface temperature distribution (heat transfer surfaces are exposed to uniform fluid temperature throughout); but complex thermal and hydrodynamic interactions at microscale result in severe flow boiling instabilities (flow reversal, parallel channel instability, temperature/pressure fluctuation, dry-out, premature critical heat flux (CHF), etc.). These instabilities are the potential impediments to the practical implementation of MCHSs. The major causes of these instabilities and their effects on the performance of MCHSs have been widely

3

studied by various researchers. Qu and Mudawar [21] studied the flow boiling of water in an MCHS containing 21 rectangular microchannels (W_{ch} = 0.231 mm and H_{ch} = 0.713 mm). They reported two types of flow boiling instabilities: severe pressure drop oscillation and mild parallel channel instability. They suggested that a severe pressure drop oscillation intensity, which leads to premature CHF, can be eliminated by throttling the flow upstream of the heat sink. Steinke and Kandlikar [22] noticed reverse expansions of vapor bubbles in microchannels and the occurrence of a complete channel dry-out - in their experimental study on six parallel microchannels (W_{ch} = 0.214 mm and H_{ch} = 0.2 mm). They reported that flow reversal is caused by the presence of parallel microchannels which offer the path of lower flow resistance during rapid bubble growth. Kandlikar et al. [23] concluded that flow instabilities can be removed by the combined influence of enhanced heat transfer and throttling at the inlet of the microchannel. They observed stabilized flow boiling in six rectangular parallel microchannels (W_{ch} = 1.054 mm and H_{ch} = 0.197 mm) of a heat sink with artificial nucleation cavities and 4% pressure drop elements at the inlet of the microchannels; however, the overall pressure was 2.4 times lower compared to that of the base case. Kosar et al. [24] experimentally verified that severe temperature and pressure drop fluctuation initiates in the conventionally designed MCHS after the inception of the boiling process. These flow boiling instabilities were suppressed by the introduction of flow distributive pillars and small orifices in their experimental study on a five parallel channel (L_{ch} = 1 cm, W_{ch} = 0.2 mm and H_{ch} = 0.264 mm) MCHS; moreover, they correlated the flow instabilities suppression in terms of a non-dimensional parameter – pressure drop multiplier. Peles's research group investigated the effect of reentrant cavities [25], and system pressure [26] on flow boiling instabilities in MCHSs. Lee et al. [27] used inlet orifices and expanding microchannels heat sink designs to suppress flow boiling instability in 48 rectangular microchannels (W_{ch} = 0.235 mm and H_{ch} = 0.710 mm). Balasubramanian et al. [28] suggested a stepped (height wise stepping in flow direction) fins MCHS to avoid flow boiling instabilities at microscale; they did not observe any flow reversal. Law and Lee [29, 30] converted 40 straight microchannels into oblique fins, they observed that wall temperature gradients and pressure fluctuation were lower for the oblique finned MCHS compared to a straight MCHS. Gao and Bhavnani [31] proposed backward and forward facing stepped geometries by modifying the side walls of a 34 parallel MCHS. They observed that the presence of steps offers effective mixing and enhances heat transfer performance by 30 - 100% with an additional pressure drop penalty of 30-70%, compared to a parallel MCHS. Raj et al. [32] compared flow boiling performance of a

4

parallel MCHS with that of a novel stepped converging MCHS. The stepped converging MCHS with 9 microchannels is fabricated with a V grove at the base of the microchannel and a converging microchannel at the top, which results in 38% higher heat transfer surface area while maintaining the same hydraulic diameter. They found that the new design results in reduction of flow boiling instabilities by enhancing the performance of the flow passage.

Uneaven distribution of working fluid in parallel channels (flow maldistribution) is one of the critical issues associated with the MCHS. Apart from temperature non-uniformity, it induces thermo-mechanical stresses. Furthermore, the presence of flow maldistribution and the associated temperature non-uniformity play a crucial role in triggering flow boiling instabilities in MCHSs that have a large number of parallel channels. The effect of flow maldistribution on single-phase flow in MCHSs has been widely explored by various researchers [33-46], mainly through numerical simulation, by changing the manifold design, or by changing the flow through it (side inlet, front inlet, top inlet and their combination). Nevertheless, very limited studies have been performed to analyze the effect of flow non-uniformity on the two-phase flow boiling process. In majority of the previous flow boiling studies realistic setbacks of flow maldistribution have not been observed due to following reasons: (1) lesser number of parallel microchannels (N ≤ 10 [22-24, 47-49]) in an MCHS and (2) large manifold size [4, 11, 21, 27-30, 50-53]. However, in practical applications, an MCHS possesses a large number of parallel channels to cover even a small base area equivalent to the size of a microprocessor. Similarly, the accommodation of the large size manifolds (length/depth) used in laboratory-scale experiments may not be obtainable in many practical applications due to space constraints. Also, a reversing vapor core condenses instantly as it enters large size manifold during subcooled boiling. Hetsroni et al. [54, 55] were among the first researchers to compare flow boiling in MCHSs with a side inlet and eccentric front inlet flow configuration by limiting manifold depth to equal microchannel depth. They found lower maximum temperature for the front inlet design and a uniform spanwise temperature distribution for the side inlet design. In another study the same authors reported that flow reversal in some of the channels alters the flow distribution of neighboring channels [56]. Wang et al. [57] experimentally investigated the effect of different flow configurations (top inlet, front inlet, and front inlet with inlet restrictions) on flow boiling in an MCHS with eight trapezoidal microchannels (D_h = 0.184 mm and L = 30 mm) and limited manifolds depth. They noticed that the way fluid entered the channels influenced flow boiling instabilities. The severity of this maldistribution was

5

highest for the top inlet type design, whereas stable flow boiling operation was observed in the design with inlet restrictions. Bogojevic et al. [58] experimentally investigated flow boiling instabilities in an MCHS with 40 rectangular microchannels (W_{ch} = 0.15 mm and H_{ch} = 0.273 mm), triangular inlet/outlet manifolds and limited manifold depth. They observed different flow regimes in the transverse direction of parallel microchannels. Ritchey et al. [59] studied the effect of non-uniform heating on the performance of an MCHS during flow boiling. They observed that with the increase of heating the non-uniformity in the transverse direction flow boiling occurred at the location where most heat was supplied, while flow remained single-phase at the location of uniform heating. Some researchers have investigated the effect of thermal coupling among parallel microchannels on two-phase flow boiling. Flynn et al. [60, 61] established that increasing thermal resistance between two parallel channels strongly influences the onset of instabilities and adversely increases the peak temperature. Van Oevelen et al. [62] theoretically investigated the effect of thermal coupling on fluid flow distribution during flow boiling by accounting axial and lateral wall conduction. They predicted that the presence of strong thermal coupling would result in redistribution of heat from the flow starved channel to the channel with excess flow, which would reduce the severity of flow maldistribution. An experimental investigation has also been carried out by the same research group [63] to study the effect of thermal coupling in two parallel microchannels.

In the previous studies, it was observed that the explosive nature of flow boiling at micro-scale triggers various flow boiling instabilities. These flow boiling instabilities generate many undesirable impacts, such as high fluctuations of temperature and pressure; they may even incept the condition of premature critical heat flux (CHF). The presence of severe flow maldistribution induces the early occurrence of flow boiling instabilities as some channels face the explosive flow boiling process due to the cooling fluid starvation problem. What is more, in studies on flow maldistribution in multiple parallel microchannels the analysis of flow patterns and temperature distribution is missing, as in Refs. [54-57]. Although, Ref. [58] discusses both transverse temperature distribution and flow patterns for top inlet flow configuration with triangular inlet and outlet manifolds, the analysis of vapor backflow with neighboring channels and systematic analysis of flow boiling propagation in the transverse direction is not covered. Furthermore, no study has systematically analyzed the temperature and flow patterns distribution in the transverse and axial direction for multiple MCHSs with an I-type flow configuration [42]. Moreover, studies

6

on two channels [60, 63] certainly mimic the idea of flow maldistribution during flow boiling; however, the extent will not be as adverse as that faced in the case of an MCHS with a large number of microchannels. Therefore, understanding the setbacks of flow maldistribution during flow boiling in parallel MCHSs, and its effect on temperature distribution as well as flow patterns is very important. In the current experimental study the negative effect of flow maldistribution on the performance of an MCHS during flow boiling is studied on an I- type configuration, with a dedicated flow visualization for central (cooling fluid rich) and side (cooling fluid starved) microchannels. What is more, an effort is made to understand the interaction between a vapor core generated through the flow reversal process and microchannels observing weak or stable flow.

2. Experimental setup and procedure

2.1 Experimental setup

A schematic diagram of the experimental setup is shown in Fig. 1 and the corresponding photograph is shown in Fig. 2. The experimental setup comprises a microchannel heat sink, a gear pump, a mass flow meter, constant temperature baths, a degassing tank, pressure transducers, thermocouples, an autotransformer, a data acquisition system, and a high-speed camera. A micro gear pump (mzr-7205, HNP Mikrosysteme) with a flow rate range of 0.047 to 288 ml/min is used to deliver degassed water to the test section. Degassing is carried out by vigorously boiling the water in a stainless steel (SS-304) tank with two embedded water immersion heaters (2×3000 W). A constant temperature bath is connected behind the degassing unit so that water can be instantly cooled after the degassing operation. A filter of 5µm pore size is connected after the constant temperature bath to restrict any solid impurities from entering the gear pump and other instruments. A Coriolis mass flow meter (M14-AGD-22-0-S, BRONKHORST CORI-Tech) with a measuring range of 10-500 ml/min is connected following the pump to measure the liquid mass flow rate. Another constant temperature bath is connected between the mass flow meter and the test section to maintain constant temperature at the inlet to the test section. Water coming from the outlet of the test section is collected in an open tank. The test section heating is controlled by an AC (0-240 V) autotransformer power supply, the heat input is measured in terms of voltage and current by a multifunction meter (RISH delta POWER). K-type thermocouples are used to measure inlet and outlet water temperatures as well as the temperature of the heat sink base. Two absolute pressure transducers (OMICRON U3221-6-002BC), with a measuring range of -1 to 1 bar, are

7

used to measure inlet and outlet pressure. A high-speed camera (Phantom V311) is used to capture the flow boiling phenomenon, and a laser light source (STORK Laser 3000) is used to provide illumination during the flow visualization. Flow visualization videos are taken at the speed of 1000 and 2000 fps for central and side microchannels. The test section is mounted on a 3-axis movement slider (HOLMARC) which facilitates smooth operation when filming flow boiling at different locations without disturbing the placement of the camera and lighting. A data acquisition system (Agilent 34792A) is used to store and transmit readings from all sensors to the interfaced PC.

2.2 Test section design

The test section consists of four parts: an MCHS, PTFE housings, a cover plate and cartridge heaters. The MCHS is made on the top face (25×25 mm) of an OFC copper block by cutting twenty-five rectangular microchannels with a wire EDM machine (Electronics Ultra cut F-2). The MCHS is embedded in the PTFE housings (upper and bottom), as shown in Fig. 3. The inlet and outlet manifolds as well as the housing for the MCHS are made on the upper PTFE, whereas the bottom PTFE helps in holding the copper block and minimizing its loosing heat to the surroundings. Inlet and outlet lines consist of two manifolds: a deep manifold ($M_{1,in}$, $M_{1,out}$) and a shallow manifold ($M_{2,in}$, $M_{2,out}$). These two manifolds are linked with each other by a connecting line (cl_{in}, cl_{out}). To measure inlet and outlet temperature as well as pressure there are holes drilled in the inlet and the outlet of the deep manifolds, as shown in Fig. 3. The top of the test section is sealed with a transparent polycarbonate (Lexan) cover plate which retains the visibility of the boiling process and insulates the top surface of the MCHS. A thin silicon gasket (thickness = 0.2 mm) is used between the upper PTFE housing and the polycarbonate plate to make the assembly leak-proof. Heating of the MCHS is carried out by inserting four cartridge heaters (4×250 W) at the bottom of the MCHS. All the cartridge heaters are connected in parallel to the autotransformer. Highly conductive thermal paste is applied to the interface between the heaters and copper substrate to reduce contact thermal resistance.

Six K-type thermocouples (three from each side) of 0.5 mm diameter are inserted at a 2.5 mm distance from the top surface of the MCHS to measure temperature distribution inside the MCHS; from which: three thermocouples are installed to measure the temperature of the central channel, and the other three thermocouples are mounted to measure the temperature right below the centerline of the 2nd microchannel. The location of the thermocouple holes are shown in Fig. 3.

8

2.3 Experimental procedure

Before each flow boiling experiment, water is fully degassed during a rigorous boiling process in the degassing unit, following the procedure described by Steinke and Kandlikar [64]. The constant temperature water bath is set at the desired water inlet temperature and the gear pump is switched on to regulate the desired flow rate through the heat sink. Once the inlet conditions are stable, electric power of the cartridge heaters and data recording systems are turned on. After the system has attained a steady state, videos visualizing the flow are made. Temperature and pressure data are recorded at an interval of 1 second. In the current study four mass fluxes: G = 99, 197, 295 and 392 kg/m^{2}s are studied for a wide range of heat fluxes. The inlet water temperature is kept at 30 and 60 ^{o}C.

3. Data reduction

3.1 Heat transfer calculation

Heat supplied (q) to the cartridge heaters is calculated by the supplied electric voltage (V) and the current (I) during experiments using eq. (1).

$$q = VI \tag{1}$$

A few percent of the heat supplied by the cartridge heaters is lost to the surroundings through heat transfer. The net effective heat transferred to the test section is calculated as:

$$q_{eff} = q - q_{loss} \tag{2}$$

Where, q_{loss} is the heat loss to the surroundings from the test section.

The heat loss is calculated by performing single-phase heat transfer experiments at different mass flow rates and heat fluxes.

$$q_{loss} = q - \dot{m}c_p(T_{f,out} - T_{f,in}) \tag{3}$$

Where, $\dot{m}$, $T_{f,in}$ and $T_{f,out}$ are mass flow rate, fluid inlet temperature and fluid outlet temperature, respectively. The heat loss varied from 6% to 9% in the current study.

Effective heat flux at the base of the MCHS (q''_{eff}) is calculated using Eq. (4).

$$q''_{eff} = \frac{q_{eff}}{A} \tag{4}$$

9

Where, A is the base area of the heat sink ($W_{HS} \times L_{HS}$).

Mass flux (G) is calculated using Eq. (5)

$$G = \frac{\dot{m}}{N\, W_{ch} H_{ch}} \tag{5}$$

As it is not possible to measure the base temperature of microchannels directly, it is interpreted by assuming one dimensional heat conduction from the level of thermocouples. Thus, the microchannel base temperature reading ($T_{w,(x,y)}$) corresponding to the thermocouple location (x,y) can be estimated in terms of the thermocouple reading at that location $T_{b,(x,y)}$ and effective heat flux q''_{eff} following Eq. (6).

$$T_{w,(x,y)} = T_{b,(x,y)} - \frac{q''_{eff} z1}{k} \tag{6}$$

Where: z1 is the distance of the microchannels' base from the thermocouples' tip, whereas x belongs to transverse coordinates for central thermocouples (x = 1) and side thermocouples (x = 2), y corresponds to stream wise positions (y = 1, 2 and 3 for three axial locations). For instance, $T_{(1,1)}$, $T_{(1,2)}$ and $T_{(1,3)}$ correspond to the temperature measurement in central microchannels along the streamwise direction at three locations. The same measurement locations are referred to as T_{cen1}, T_{cen2} and T_{cen3}, respectively in all the Figures to provide more clarity. Similarly, $T_{(2,1)}$, $T_{(2,2)}$ and $T_{(2,3)}$ refer to the temperature measurement along the streamwise direction in side microchannels; and for better understanding, similar nomenclature - T_{side1}, T_{side2} and T_{side3} - is adopted in the Figures.

3.2 Pressure drop measurement

In the current study pressure is measured at the inlet and the outlet deep manifold, their difference gives the pressure drop across the entire assembly, as calculated in Eq. (7).

$$\Delta P = P_{in} - P_{out} = \Delta P_{in} + \Delta P_{ch} + \Delta P_{out} \tag{7}$$

$$\Delta P_{ch} = \Delta P - \Delta P_{in} - \Delta P_{out} \tag{8}$$

Where ΔP_{in}, ΔP_{ch} and ΔP_{out} represent pressure losses in the inlet section, microchannels and the outlet section. Inlet and outlet sections contain two manifolds and a connecting line, as shown in Fig. 3. Fluid first enters the deep inlet manifold, ($M_{1,in}$ in Fig. 3) where an inlet pressure reading is recorded. After flowing through the deep manifold, the fluid experiences a sudden contraction

10

as it enters the connecting line (cl_{in}). The fluid again experiences a sudden expansion as it enters the shallow manifold ($M_{2,in}$), after flowing through the connecting line. The fluid experiences significant flow friction in the connecting line; and in the shallow manifold it experiences major fluid friction loss, as well as minor fluid friction loss, due to a sudden contraction effect as the fluid enters microchannels. Similarly, the fluid experiences counterwise hydraulic resistances in the outlet manifolds and in the connecting line. Total pressure drop in the inlet and outlet section is calculated using Eqs. (9) and (10), respectively.

$$\Delta P_{in} = \Delta P_{M1,in} + \Delta P_{c,cl,in} + \Delta P_{cl,in} + \Delta P_{e,M2,in} + \Delta P_{M2,in} + \Delta P_{c,ch,in} \tag{9}$$

$$\Delta P_{out} = \Delta P_{e,ch,out} + \Delta P_{M2,out} + \Delta P_{c,cl,out} + \Delta P_{cl,out} + \Delta P_{e,M1,out} + \Delta P_{M1,out} \tag{10}$$

$\Delta P_{M1,in}$, $\Delta P_{c,cl,in}$, $\Delta P_{cl,in}$, $\Delta P_{e,M2,in}$, $\Delta P_{M2,in}$, and $\Delta P_{c,ch,in}$ are friction losses in $M_{1,in}$, contraction losses in cl_{in}, friction losses in cl_{in}, expansion losses in $M_{2,in}$, friction losses in $M_{2,in}$ and contraction losses at the entrance of microchannels, respectively. Similarly, $\Delta P_{e,ch,out}$, $\Delta P_{M2,out}$, $\Delta P_{c,cl,out}$, $\Delta P_{cl,out}$, $\Delta P_{e,M1,out}$ and $\Delta P_{M1,out}$ represent expansion losses at the outlet of microchannels, friction losses in $M_{2,out}$, contraction losses in cl_{out}, friction losses in cl_{out}, expansion losses in $M_{1,out}$ and friction losses in $M_{1,out}$. The calculation of all pressure drop components is carried out following Refs. [21, 65]; the calculation procedure for all the pressure drop components is given below:

All pressure losses caused by sudden contraction ($\Delta P_{c,cl,in}$, $\Delta P_{c,ch,in}$ and $\Delta P_{c,cl,out}$) are calculated using Eqs (11) – (13).

$$\Delta P_{c,cl,in} = \frac{1}{2}\rho_f\left(u^2_{cl,in} - u^2_{M1,in}\right) + \frac{K_{c1}}{2}\rho_f u^2_{cl,in} \tag{11}$$

$$\Delta P_{c,ch,in} = \frac{1}{2}\rho_f\left(u^2_{ch,in} - u^2_{M2,in}\right) + \frac{K_{c2}}{2}\rho_f u^2_{ch,in} \tag{12}$$

$$\Delta P_{c,cl,out} = \frac{1}{2}\rho_f\left(u^2_{cl,out} - u^2_{M2,out}\right) + \frac{K_{c3}}{2}\rho_f u^2_{cl,out} \tag{13}$$

Where, K_{c1}, K_{c2}, and K_{c3} are loss coefficients for sudden contraction. Values of loss coefficient are taken from Ref. [66].

Components of pressure losses due to sudden expansion ($\Delta P_{e,M2,in}$, $\Delta P_{e,ch,out}$ and $\Delta P_{e,M1,out}$) are calculated using Eqs (14) – (16).

$$\Delta P_{e,M2,in} = \frac{1}{2}\rho_f\left(u_{M2,in}^2 - u_{cl,in}^2\right) + \frac{K_{e1}}{2}\rho_f u_{M2,in}^2 \tag{14}$$

$$\Delta P_{e,ch,out} = \frac{1}{2}\rho_f\left(u_{M2,out}^2 - u_{ch,out}^2\right) + \frac{K_{e2}}{2}\rho_f u_{ch,out}^2 \tag{15}$$

$$\Delta P_{e,M1,out} = \frac{1}{2}\rho_f\left(u_{M2,out}^2 - u_{M1,out}^2\right) + \frac{K_{e3}}{2}\rho_f u_{M1,out}^2 \tag{16}$$

Similarly, K_{e1}, K_{e2}, and K_{e3} are loss coefficients for sudden expansion. These are calculated as follows: $K_{e1} = (1 - \frac{A_{cl}}{A_{M2}})^2$; $K_{e2} = (1 - \frac{A_{ch}}{A_{M2}})^2$; $K_{e3} = (1 - \frac{A_{cl}}{A_{M1}})^2$.

All major friction losses include hydrodynamic developing flow in the inlet and outlet sections ($\Delta P_{M1,in}$, $\Delta P_{cl,in}$, $\Delta P_{M2,in}$, $\Delta P_{M2,out}$, $\Delta P_{cl,out}$, and $\Delta P_{M1,out}$) as well as fully developed laminar flow in the microchannels (ΔP_{ch}).

The pressure drop in the developing regions is calculated in terms of the apparent friction factor (f_{app}) using Eq. (17).

$$\Delta P_d = \frac{2f_{app}\,L_d\,u_d^2\,\rho_{f,d}}{D_h} \tag{17}$$

Where f_{app} is calculated using Eq. (18) [65].

$$f_{app} = \frac{1}{Re_d}\left(3.44\,{L_d^*}^{-0.5} + \frac{\frac{1.089}{4L_d^*} + f_d Re_d - 3.44\,{L_d^*}^{-0.5}}{1 + 1.31\times10^{-4}\left(L_d^*\right)^{-2}}\right) \tag{18}$$

Where L_d^* is the non-dimensional length of a single-phase developing sub region ($L_d^* = \frac{L_d}{Re_d D_h}$), the friction factor for the developing region (f_d) is calculated by using Eq. (19) [65] and $Re_d = \frac{\dot{m}D_h}{\mu_d}$.

$$f_d = \frac{24}{Re_d}(1 - 1.3553\alpha + 1.9467\alpha^2 - 1.7012\alpha^3 + 0.9564\alpha^4 - 0.2537\alpha^5) \tag{19}$$

Similarly, the pressure drop of a fully developed region is calculated using Eq. (20) [65].

$$\Delta P_{fd} = \frac{2f_{fd}L_{fd}u_{fd}^2\rho_{fd,ave}}{D_h} \tag{20}$$

Where the friction factor for the developing region (f_{fd}) is calculated using Eq. (21) [65], $\alpha = \frac{W_{ch}}{H_{ch}}$ and $Re_{fd} = \frac{\dot{m}D_h}{\mu_{fd}}$.

$$f_{fd} = \frac{24}{Re_{fd}}(1 - 1.3553\alpha + 1.9467\alpha^2 - 1.7012\alpha^3 + 0.9564\alpha^4 - 0.2537\alpha^5) \qquad (21)$$

3.3 Uncertainty analysis

Thermocouples and the mass flow meter are calibrated in the lab. The uncertainty associated with the K-type thermocouples used in the present study equals ± 0.6 °C. Whereas the maximum error associated with the measurement of mass flow rate is ±2%. The uncertainty in the pressure transducers, according to the certificate provided by the manufacturer, is ±0.5% of the full scale of the measured value. At the same time, the uncertainty associated with the measurement of the current and voltage equals ±1% of the measured value; and the uncertainty associated with the measurement of the microchannels' width and depth is ±10 µm. The uncertainty associated with various derived parameters is calculated by adopting the procedure given in [67]; the uncertainty is presented in Table 2.

4. Results and discussion

4.1 Validation

The validation of current experimental results is carried out by comparing them with well accepted correlations for Nusselt number [68] and pressure drop (Eq. 7) in single-phase flow, as shown in Fig. 4. A mean absolute deviation of 11% and 16.8% is observed in the calculation of Nusselt number and pressure drop, respectively, with respect to the correlations. The calculation of two-phase pressure drop with various two-phase correlations was discussed in detail by Qu and Mudawar [21]. To calculate total pressure drop, the length of microchannels is divided into a single-phase region ($x_e < 0$) and a flow boiling region ($x_e > 0$). For the region of $x_e < 0$ pressure drop is calculated by using single-phase methods, as explained in the subsection 3.2. Two-phase pressure drop in the region of $x_e > 0$ is calculated by adopting various two-phase pressure drop correlations. In the present study $x_e < 0$ for the entire studied range of working conditions. It is due to severe flow maldistribution which results in a highly asymmetric nature of flow boiling propagation in parallel microchannels. Therefore, validation of pressure drop cannot be performed

with the saturated flow boiling correlation. Similar challenges were faced by Lee and Mudawar [69] during their experimental study on subcooled flow boiling in microchannels; thus, a correlation proposed by Lee and Mudawar [69] is used, to calculate heat transfer during subcooled flow boiling in microchannels, the results are shown in Fig. 4 (c). A mean absolute error (MAE) of 12.3 % is observed and all data falls within ±30% of predicted values for the entire working conditions, which shows the reliability of observations made during the current experiments.. Moreover, the pressure drop during subcooled flow boiling is validated following the method of normalizing the two-phase pressure drop relative to adiabatic flow [70]. The ratio of $\Delta P/\Delta P_{ad}$ is compared with the correlation of Tong et al. [71], the results are shown in Fig. 4 (d). A MAE of 23.5% is noticed and 86% of the experimental readings fall within an error ±30% of predicted values.

4.2 Repeatability test

Repeatability of experimental results is tested by repeating the experiments for a wide range of heat fluxes at $G = 295$ kg/m^{2}s and $T_{in} = 30$ ^{o}C, as shown in Fig. 5. It is found that trends in temperature and pressure drop profiles are repeatable in nature with a maximum deviation of 2.4 ^{o}C and 417 Pa in the boiling curve and pressure drop, respectively.

4.3 Boiling curve

Figure 6 shows the boiling curve for $G = 295$ kg/m^{2}s and $T_{in} = 30$ ^{o}C. In the boiling curve temperature readings of all the locations are plotted in order to understand temperature distribution in the MCHS. Any type of non-uniformity (boundary conditions and mass flow distribution) generates disastrous impact on the performance of the MCHS [72]. Side channels face two undesirable effects: i. They receive less coolant fluid mass in comparison to central channels (for the I-type MCHS) [8], and ii. Weak heat transfer boundary condition (warm air natural convection boundary conditions). Therefore, the temperature of side microchannels surges rapidly in comparison to that of central channels. The combined effect of low mass flux and high wall temperature ($\Delta T_{sup} \sim 5$ ^{o}C near outlet) leads to the inception of flow boiling in side microchannels at $q''_{eff} = 64.9$ W/cm^2. At this condition a very rapid growth of bubbles is noticed in the 1st and the 2nd microchannel, whereas a weak, stable, bubbly flow is observed in the neighboring channels. The rapid bubble growth in the 1st and the 2nd microchannel instantly leads to periodic flow reversal

14

of vapors up to the inlet manifold in these channels. This condition is marked as the onset of flow reversal (OFR) instability for the side microchannels (1st and 2nd).

It can be noticed that the slope of all thermocouples is fairly constant during single-phase flow. After the occurence of ONB in side microchannels (ONB$_{side}$), the slope of the boiling curve abruptly increases for the terminal thermocouple $T_{w(2,3)}$, as a vapor bubble incepts in the latter half of side channels (subcooled boiling). Due to the subcooled boiling process, the vapor bubble incepts towards the downstream side (near the exit of the outlet manifold). Despite the fact that the flow in the central channel remains single-phase at ONB$_{side}$, the behavior of $T_{w(1,3)}$ indicates that it starts experiencing the benefits of intensified heat transfer due to the strong 3D conjugate two-phase heat transfer effect in the MCHS. The influence of the above extends up to the central part of the MCHS ($T_{w(2,2)}$ and $T_{w(1,2)}$). However, no significant difference is observed in the slope of the initial thermocouples ($T_{w(2,1)}$ and $T_{w(1,1)}$). As the applied heat flux is increased, the flow boiling intensity increases and more parallel microchannels (towards the center most channel) start experiencing rapid bubble growth. At $q''_{eff} = 69.1$ W/cm^2 the first vapor bubble inception becomes visible in the center most microchannel. It is represented by ONB$_{cen}$ in the boiling curve. Bubbles nucleate near the center of the center most channel and slide along the walls of channels in line with the flow direction. The size of the bubbles remains relatively small due to the high flow rate of subcooled fluid, where the evaporation process is perhaps dominated by condensation. At q''_{eff} = 70.8 W/cm^2 multiple nucleating bubbles are seen near the outlet of the center of most channels as well. Surprisingly, no flow reversal is observed in the central channel at the ONB$_{cen}$. With further increase in heat flux, the bubble nucleation activity certainly increases, but the flow in the central channel remains a stable bubbly flow. Even at the highest studied heat flux, rapid growth of vapor bubbles in central channels (caused by a growing bubble confining the microchannel) is not observed. Rapid bubble growth in central channels seems to be delayed under the influence of mirage flow confinement (q''_{eff} = 79.2 W/cm^2) and mirage flow reversal ($q''_{eff} \geq 83.4$ W/cm^2). Mirage flow confinement and mirage flow reversal are occurrences of flow confinement and flow reversal initiated by a vapor core which is originally developed in side microchannels and transferred to the central channel due to a strong flow reversal, as shown in Fig 7. This ephemeral vapor core is generated by the vapor backflow Type 3 (explained in Sec. 4.4). Flow pattern transitions in the various microchannels are discussed in detail in the following section.

4.4 Flow visualizations

Distinct flow boiling patterns can be easily distinguished at macroscale, but in microchannels flow patterns are associated with transient fluctuations of flow regimes. Therefore, dedicated investigations of transient flow regimes at different axial locations are required. What is more, in order to analyze a flow pattern in different parallel microchannels, it is essential to obtain flow visualization results at different transverse locations among parallel microchannels. Thus, in the current study flow patterns are captured at two axial (near the inlet and the outlet of microchannels) and two transverse (side and central microchannels) locations.

As discussed in section 4.3, flow maldistribution results in a very rapid bubble growth only in side microchannels ($i = 1$ and 2). Figure 8 shows the alternation of different flow patterns near the outlet of the 2nd microchannel at $G = 295$ kg/m^{2}s and $q''_{eff} = 64.9$ W/cm^2. The direction of the flow is from left to right. At $t = 0$ s multiple small vapor bubbles are noticed, which nucleate from the side walls as well as from the base of the microchannel. The intensity of bubbles nucleation and their growth is found larger at the common edges of heating sides (at the corners) in comparison to the free flow stream. Also at that edges fluid velocity vectors (responsible for drag and lift forces) are minimual. Thus, they act as the preferred location for the formation of nucleation sites. Less than ten percent of the bubble population develops away from the common intersecting edge or in the neighboring area. It is noticed that with time the number of bubbles and their size both increase, which results in the channel flow passage confinement caused by a growing vapor bubble (at $t = 0.051$ s). The initial confinement promotes rapid bubble growth in the upstream part, instantly a blockage of the channel cross-section is noticed at three locations ($t = 0.052$ s). Vapor bubbles trapped between the two confined bubbles experience fast growth unlike the remaining upstream bubbles. A confined vapor bubble turns into small vapor plugs through individual growth as well as through merging with neighboring bubbles (Fig. 8 (d)). Subsequently, due to the growth and merging of these small vapor plugs, a vapor slug is formed, and it covers the entire downstream region (Fig. 8 (e)). This vapor slug slowly starts growing in the upstream direction (Fig. 8 (f)). But before it grows further, another upstream growing plug compresses and then merges with a bigger slug in the downward direction (Fig. 8 (g) – (h)). Eventually, they cover the entire length of the microchannel (Fig. 8 (i)). Similarly to these entrapped vapor bubbles, upstream confined vapor bubbles also experience rapid bubble growth in the absence of liquid inertial force. At $t = 0.072$ s,

as the elongated bubble covers the entire channel length, the flow pattern resembles the annular flow regime with a continuous, confined vapor bubble in the channel core and a thin liquid layer separating the vapor interface from the microchannel walls. With time the thin liquid film evaporates, which results in the condition of a partial dry-out at the microchannel walls ($t = 0.114$ s). At $t = 0.162$ s the clogged channel begins to clear off with an incoming stream of fresh liquid. It is observed that as the clogged vapor is pushed in the downstream direction, bubble nucleation happens in the upstream part Fig. 8 (l). Fig. 8 (m) resembles the beginning of the cycle (Fig. 8 (a)); after which the complete cycle repeats itself. In their experimental study on triangular microchannels Hetsroni et al [56] observed a similar rapid bubble growth phenomenon. They reported that at the onset of boiling the bubble grew rapidly and occupied the entire channel.

It is observed that the flow regimes described in Fig. 8 appear in the 1st and the 2nd microchannel. The upstream end of the elongated vapor periodically reaches the inlet of the 1st and the 2nd microchannel, due to flow reversal; then it tries to extend to the manifold inlet, but it condenses instantly as it comes in contact with the subcooled liquid. Also, the vapor core tries to expand again, in that case condensation extends up to a certain length of the confined channel. Hence, a slight back and forth motion is observed as the vapor slug length reaches the microchannel inlet of (at $q''_{eff} = = 64.9$ W/cm^2). As the projected area of side channels in the inlet manifold remains a stagnant zone (due to fluid recirculation), it supports the momentary survival of the expanding vapor core. It causes a periodic change of flow rate in the downstream region of the microchannel, and leads to alternating flow regimes in the downstream region of the microchannel.

Compressibility of the vapor slug and liquid are both observed even from the downstream side . These phenomena are explained in Fig. 9 and shown in Supplementary Video 1. Low pressure zones are created on the exit of several vapor blocked channels, due to uneven pressure distribution among parallel channels. As fluid from a neighboring microchannel (experiencing single-phase flow) diverts towards such a microchannel and starts compressing the vapor core of that channel ($i = 1 - 3$ in Fig. 9 (a) – (c)). As a result, an intermittent backflow of a confined vapor patch near the channel outlet is noticed, which consistently disturbs the annular flow near the channel outlet region. This consistent disruption helps to keep wet conditions near the channel outlet, despite the presence of intermittent dry-out zones in the upstream direction of the microchannels (Fig. 9).

However, unlike the upstream flow compressibility, the intensity of downstream flow compressibility is low. It is also observed that the vapor core leaving the microchannel compresses the liquid core of the neighboring channel, this results in a momentary reverse flow ($i = 4$ in Fig. 9 (e) – (g)) which is then superseded by the upward stream of fresh liquid (Fig. 9 (h)).

It is observed that with a slight increment of heat flux (at $q_{eff}'' = 67.3$ W/cm^2) the intermittent annular flow region expands to all 5 side microchannels resulting in a sudden drop of the substrate temperature, as observed in the boiling curve. The observed behavior seems to be due to an abrupt increase in the nucleate boiling effect in the MCHS; the subsequent dominance of the convective boiling effect pulls the temperature up again, with further increase in heat flux. It is also noticed that at lower heat flux coalescences of multiple bubbles play a vital role in flow reversal, as depicted in Fig. 10 (a); however, at higher heat flux a bubble after nucleation undergoes very rapid growth Fig. 10 (b). It is expected that the density of nucleation sites should be higher in the situation of high heat flux; but in a microchannel at high heat flux growing vapor bubbles block the channel at several sites, and start rapidly covering the high energy sites which can act as nucleation sites for the development of new, tiny vapor bubbles. These high energy density sites actively contribute to and convert the growth of vapor bubbles from fast to rapid. That is why on both occasions (Fig. 10 (a) and (b)), even though the complete channel confinement occurs following the fluid flow reversal, a bubble takes only one third of time to cover the entire length at high heat flux. Furthermore, the intensity of backflow in the upstream part of the associated microchannel strengthens with the increase in heat flux as the vapor patch starts covering a bigger area of the inlet manifold. As a result, the inlet of more microchannels gets covered, which hampers the flow supply of those channels. It is observed that at $q_{eff}'' = 64.9$ W/cm^2 for ~70% of time (out of 1 s duration) single-phase liquid flow or liquid flow with a few small bubbles without any blockage is observed near the inlet of all 5 side microchannels, and this percentage is reduced to ~13% at $q_{eff}'' = 67.3$ W/cm^2. As the number of microchannels facing flow reversal increases, the mass flow rate through neighboring channels increases; that is supposed to delay the occurrence of flow reversal in neighboring channels by promoting more vapor bubble dislodging from nucleation sites, as shown in Fig 11. It is observed that as flow reversal is initiated in channels 1st and 2nd (Fig. 11 (c)) the size of bubbles in the neighboring microchannels diminishes in comaprison to the situation of no flow reversal (Fig. 11 (a – b))). At $q_{eff}'' = 69.1$ W/cm^2 a stable bubbly flow

18

is noticed near the outlet of the center most microchannel. However, the size of bubbles in central microchannels remains relatively small as it has the benefit of the central location biased flow rate.

While analyzing vapor backflow in the inlet manifold, three types of interactions are observed mainly:

Type 1: back and forth motion near channel inlet.

Type 2: back and forth motion near channel inlet and interaction with neighboring microchannels.

Type 3: back and forth motion near channel inlet and interaction with central microchannels.

At the inception of flow boiling, only Type 1 mechanism is observed, where vapor backflow does not block the inlet of neighboring microchannels as they rapidly condense on the impending subcooled liquid approaching the microchannel inlet. With the increase in heat flux, more channels start experiencing the alternating, bubbly/annular flow; therefore, more than one channel ($i = 1$ and 3 in Fig. 12) starts experiencing synchronized (with a slight time lag) flow reversal (Type 2). As the mass of vapor transferred back to the manifold increases, the vapor core does not condense instantly on entering the manifold and tries to drift away towards neighboring microchannels associated with lower operating pressure ($i = 2$ and 4). When the approached channel is experiencing single-phase or weak bubbly flow on one side then, despite heavy replenishing of vapor from one side of the neighboring channel, the condensation originating from the other side leads to an early disappearance of the generated vapor core. On the other hand, if the approached microchannel is covered by the adjacent microchannels' vapor core ($i = 2$ in Fig. 12 (a)) then the drifted vapor forms a stable vapor plug at the inlet of the microchannel ($i = 2$ in Fig 12 (c)). The entrapped liquid core experiences simultaneous compression and evaporation (i = 2 in Fig 12 (c); eventually, the whole channel is filled with the vapor core ($i = 2$ in Fig 12 (d)) and becomes part of flow regimes of the associated channel ($i = 2$ in Fig. 12 (e)). In the downstream direction it experiences further rapid growth as well as flow reversal, due to high superheating of the channel walls (Fig. 12 (f)).

At $q''_{eff} = 79.2$ W/cm^2 Type 3 interaction is observed, where the intensity of flow reversal in side microchannels increases to the extent that their vapor backflow reaches central microchannels, it enters the central microchannels and immediately flows downstream, as shown in Fig 13 (a). During downstream motion the elongated vapor experiences condensation, and in the downstream

19

part of central microchannels only bubbles coming from the upstream direction are noticed, as shown in Fig. 13 (a). No actual confinement or flow reversal is observed for the central channel under the studied range of heat flux. Stable bubbly flow is observed in the central channel. However, due to Type 3 interaction at $q''_{eff} = 79.2$ W/cm^2 mirage flow confinement is observed, and with further increase of heat flux ($q''_{eff} \geq 83.4$ W/cm^2) mirage flow reversal near the inlet of central channels (MFR$_{cen}$) is noticed. This phenomenon at the inlet of central microchannels ($i = 11 - 15$) is depicted in Fig. 7 and shown in Supplementary Video 2. Due to mirage confinement in central channels (Fig 13 (b)), evaporation of a thin liquid layer takes place, which results in the appearance of intermittent dry-out patches near the outlet of central channels. It leads to a prominent rise in the temperature of central channels caused by poor thermal transport properties of vapor and the intermittent disruption in the supply of fresh fluid. The intermittent dry-out patches vanish as the mirage confined channels are cleared off with fresh liquid supply. Likewise in side channels, the disruption in flow supply, due to the channels blockage caused by vapors, increases the possibility of a dry-out at the downstream locations; and as a result, a sudden surge in the temperature of side channels is also noticed. The maximum studied heat flux is limited to 89.8 W/cm^2 at mass flux $G = 295$ kg/m^{2}s as the temperature profile indicated that the operating condition reaches in the vicinity of the unsafe working limit.

4.5 Temperature distribution

Non-uniformity of the base surface temperature is the most crucial parameter, especially in subcooled boiling. It is well evident that severe temperature non-uniformity may lead to the categorical failure of the electronic circuit associated with the MCHS. To analyze the effect of non-uniform flow distribution on the temperature rise in central and side microchannels, the temperature difference in the streamwise direction (ΔT_s) is calculated for central ($\Delta T_{s,cen} = T_{w,(1,3)} - T_{w,(1,1)}$) and side ($\Delta T_{s,side} = T_{w,(2,3)} - T_{w,(2,1)}$) microchannels. In the similar context, the average temperature difference in the transverse direction ($\Delta T_{t,avg}$) is also calculated using Eq. (10).

$$\Delta T_{t,avg} = \Delta T_{side,avg} - \Delta T_{cen,avg} \tag{10}$$

Where, $\Delta T_{side,avg}$ and $\Delta T_{cen,avg}$ are the average temperature of side ($T_{side,avg} = (T_{w,(2,1)} + T_{w,(2,2)} + T_{w,(2,3)})/3$ and central ($T_{cen,avg} = (T_{w,(1,1)} + T_{w,(1,2)} + T_{w,(1,3)})/3$) microchannels.

In Fig. 14 (a) the temperature difference in the streamwise direction (ΔT_s) is compared for side microchannels ($\Delta T_{s,side}$) and central microchannels ($\Delta T_{s,cen}$) at G = 295 kg/m^{2}s and T_{in} = 30 ˚C. It is observed that $\Delta T_{s,side}$ and $\Delta T_{s,cen}$ increase with the increase of heat flux during single-phase flow on account of more localized heating in the downstream direction. $\Delta T_{s,side}$ rapidly decreases once boiling initiates in side microchannels. As initially the flow reversal intensity generated inside the side microchannels (i = 1 and 2) is weak, the vapor core condenses almost at the mouth of these microchannels. Vapor core energy generated through their condensation is transferred only to associated channels (Type 1). Hence, the $\Delta T_{s,cen}$ still increases in spite of the boiling process initiation in side channels. On increasing the heat flux, as Type 2 interaction begins, the vapor core generated through flow reversal becomes stronger to starts extending inside the inlet manifold. Therefore, the energy generated through condensation gets transferred to the upcoming liquid. Hence, $\Delta T_{s,cen}$ starts decreasing, in spite of single-phase flow continuing in the central microchannel as flow reversal in side channels initiates at ONB$_{cen}$. Certainly, the influence of a strong 3D conjugate two-phase heat transfer effect also seems to influence $\Delta T_{s,cen}$, particularly at the terminal thermocouple location (Fig. 6). It is observed that $\Delta T_{s,side}$ and $\Delta T_{s,cen}$ reduce by 72.5% and 23%, respectively, when heat flux is increased from 63.6 W/cm^2 (single-phase region) to 83.4 W/cm^2 (two-phase region). It is noticed that unlike the side microchannel, the central microchannel does not undergo the sharp/systematic temperature decrease even after ONB$_{cen}$. The presence of mirage flow confinement and resulting MFR$_{cen}$ seems to be the expected reason behind the observed trend. Furthermore, MFR$_{cen}$ also results in confined channel walls in the downstream direction of central microchannels, as discussed in section 4.4; consequently, the appearance of temporal dry-out zones and momentary disturbance in fresh liquid supply leads to localized heating of the vapor entrapped channel walls at the downstream location. As a result, a sudden temperature rise is noticed near the outlet of central channels, and accordingly, a slight rise in the $\Delta T_{s,cen}$ profile is observed at $q''_{eff} > 83.4$ W/cm^2. The unidirectional decreasing trend of $\Delta T_{s,side}$ (after ONB$_{side}$) is maintained until $q''_{eff} = 83.4$ W/cm^2; and at $q''_{eff} > 83.4$ W/cm^2 this decreasing trend ceases, which can be credited to the disruption of flow supply in side channels due to the intensification of Type 3 interactions and the possibility of an intermittent dry-out at the downstream locations. Surprisingly, $\Delta T_{s,cen}$ is found higher than $\Delta T_{s,side}$ for the entire range of heat flux; even though it receives more flow rate of the subcooled liquid than the side microchannel due to the low maldistribution effect in the I-type configuration. The difference in the subcooled fluid inlet

21

temperature arises due to the insigniffict depth of the M_2 manifold (fluid flow heating by the front wall of microchannels and their vectoring towards side microchannels [8]). The difference between $\Delta T_{s,cen}$ and $\Delta T_{s,side}$ increases as two-phase flow boiling initiates in the side microchannel. However, once the MFR$_{cen}$ condition is achieved, the difference starts decreasing due to more localized heating in the downstream direction.

Average temperature difference in the transverse direction ($\Delta T_{t,avg}$) is shown in Fig. 14 (b). It is observed that $\Delta T_{t,avg}$ increases with the increase of heat flux. The rising trend indicates that the temperature non-uniformity in the transverse direction increases with the increase of heat flux during flow boiling. The existence of this temperature non-uniformity is primarily due to the non-uniform fluid flow distribution and poor heat transfer boundary conditions of the side microchannel, which then triggers asymmetric flow boiling in the parallel microchannels. As a result, OFR$_{side}$ is observed prematurely causing the inception of dry-out zones in side microchannels as their temperature rises prominently (Fig. 6). On the other hand, the presence of the stable bubbly flow regime in central channels restricts the temperature rise of central microchannels until MFR$_{cen}$. Furthermore, as the MFR$_{cen}$ begins, a sudden temperature rise in the central channels is also noticed; however, the temperature rise is more severe in the side channels, which is responsible for the increasing trend of $\Delta T_{t,avg}$.

4.6 Effect of mass flux

The boiling curves for G = 99, 197 and 392 kg/m^{2}s are shown in Fig. 15, whereas Fig. 16 compares stream-wise ($\Delta T_{s,cen}$ and $\Delta T_{s,side}$) and transverse ($\Delta T_{t,avg}$) temperature differences at different mass fluxes. Boiling incepts at higher wall superheat with the increase in mass flux. Boiling in the MCHS, each time initiated in side microchannels (simultaneously in the two side most channels) under the influence of flow maldistribution and the drop in the $\Delta T_{s,side}$ profile, is observed at OFR$_{side}$. It is noted that at low mass flux, flow reversal becomes intense with a slight increase in heat flux. Hence, a stable vapor core is generated inside side microchannels at low heat flux. It creates a dry-out condition at the inlet of a side microchannel leading to a sharp increase in temperature of the side microchannel's first thermocouple (Type 1 to Type 2). Therefore, $\Delta T_{s,side}$ again starts rising with the increase in heat flux - beyond $q''_{eff} > 35.4$ W/cm^2 at G = 99 kg/m^{2}s. Under the influence of low mass flux, the backflow rapidly changes from Type 2 to Type 3 at q''_{eff} = 37 W/cm^2, which results in the generation of mirage confinement and flow reversal in central

channels. For the duration of time when Type 3 is absent, the flow pattern near the outlet of central channels reamains a stable bubbly flow. However, as the vapor core confines central channels (after Type 3), it results in a rapid growth of upstream vapors in these channels during the downward motion. At heat flux $q''_{eff} > 37$ W/cm², a few instances of the bubbly flow conversion to a slug flow, due to rapid bubble growth, is also observed near the outlet of central channels. This behavior is not observed for $G > 99$ kg/m²s when only the stable bubbly flow and mirage confinement are noticed. Moreover, due to the low fluid momentum more significant dry-out regions are noticed near the outlet of central channels. With further increase of heat flux, the condition of premature CHF [73] is observed at $q''_{eff} = 39.2$ W/cm². The influence is also evident while observing the change of the flow boiling curve slope at $G = 99$ kg/m²s, as shown in Fig. 15 (a). Therefore, the inception of Type 3 interaction can be considered in the vicinity of unsafe working conditions, at low mass flux conditions. At the lowest mass flow rate the maldistribution problem is not severe; thus, any flow boiling non-uniformity between the central and side channels ceases very soon.

Although flow non-uniformity increases with the increase in mass flow rate, the flow through individual channels also increases. Thus, with the increase of mass flux ($G = 197$ kg/m²s) intense boiling (conversion of bubbly flow to slug flow) is not noticed in the central channel. Therefore, the premature CHF condition is not observed at $G = 197$ kg/m²s for the studied range of heat flux. Boiling patterns between the central channel and the side channel become desynchronized. Similarly, the duration of dry-out occurring in the side channel is not longer than was observed at a low mass flow rate. Thus, subcooled liquid rewets the surface frequently after the dry-out, helping to avoid a sharp temperature rise, as observed at the mass flux of $G = 99$ kg/m²s. The behavior of $\Delta T_{s,cen}$ is found quite similar to what was observed at $G = 99$ kg/m²s. As in other cases, $\Delta T_{s,side}$ observes a sharp decrease in temperature after OFR$_{side}$ conditions.

At the onset of flow boiling, few nucleating bubbles are observed in the first microchannel for the highest studied mass flux ($G = 392$ kg/m²s). However, the simultaneous flow reversal phenomenon (OFR$_{side}$) is not observed at the same heat flux, unlike in the other cases. Therefore, $\Delta T_{s,side}$ of the side channel increases even after the inception of the boiling process at $G = 392$ kg/m²s. After increasing the heat flux, rapid bubble growth initiates ($q''_{eff} = 79.6$ W/cm²), resulting in flow reversal up to the inlet manifold (Type 1), and $\Delta T_{s,side}$ starts decreasing from this point.

Type 3 interaction has not been noticed for the entire studied range of heat flux. Rapid condensation of the vapor core (generated through flow reversal) by a high flow rate of the subcooled liquid seems to be responsible for the observed behavior. At high mass flux, the flow of subcooled liquid through the central channel increases. Thus, the influence of flow boiling in the side channel does not transfer quickly to the central microchannel, and a vapor slug (generated in the side microchannels) gets condensed inside the manifold exclusively. It is observed that $\Delta T_{t,avg}$ increases with the increase of mass flux, which is mainly due to the increase in flow distribution non-uniformity between central and side channels [42]. Furthermore, a decreasing trend of $\Delta T_{t,avg}$ is observed in lower mass flux cases (G = 99 and 197 kg/m^{2}s) after Type 3 interaction. A decrease in the trend of $\Delta T_{t,avg}$ is observed in lower mass flux cases (G = 99 and 197 kg/m^{2}s) after Type 3 interaction. The above observation is due to a sudden jump in the temperature of central microchannels at low mass flow rates after the inception of Type 3 interaction.

Fig. 17 compares flow boiling patterns in side and central microchannels at mass fluxes of G = 295 and 392 kg/m^{2}s at q''_{eff} = 83.4 W/cm^2. It is observed that for a fixed heat flux condition, the mass flux increase reduces the flow boiling intensity in side and central microchannels. It can be noticed that at G = 295 kg/m^{2}s the condition of intermittent dry-out is observed in all five side microchannels, and Type 3 interaction is present. Whereas at higher mass flux (G = 392 kg/m^{2}s) the intermittent dry-out condition is mainly observed up to the third side microchannel only, the backflow of these microchannels is also limited and could not influence the adjacent microchannels, due to a high flow momentum in the inlet manifold (Type 1). At the central part of the MCHS only nucleating bubbles are noticed near the outlet, and liquid remains in a subcooled state near the inlet.

4.7 Effect of inlet temperature

The boiling curves for T_{in} = 60 ^{o}C are given in Fig. 18. It can be noticed by comparing the boiling curves of T_{in} = 30 ^{o}C that higher inlet subcooling offers high heat flux dissipation, thus ensuring low substrate temperature maintenance. As in T_{in} = 30 ^{o}C cases, boiling initiates in side microchannels, first owning flow maldistribution between the central, side microchannels and the adiabatic outside wall conditions. It is observed that the heat flux at which flow reversal initiates (q''_{eff} = 38.7 W/cm^2) in side microchannels is reduced by ~40% for T_{in} = 60 ^{o}C compared to T_{in} = 30 ^{o}C at G = 295 kg/m^{2}s, caused by the increase in temperature of the subcooled cooling fluid. In

24

Fig. 19, the flow patterns of central and side microchannels are compared for T_{in} = 30 and 60 °C, at the inception of the flow boiling process for G = 295 kg/m²s. Similar flow patterns are observed in side microchannels for both inlet temperatures. However, it is observed that the intensity of flow boiling is higher for T_{in} = 30 °C at the inception of Type 1 interactions. It is noticed that the dominant flow regime in the 2nd microchannel is still the bubbly flow, and the intermittent annular flow pattern develops only once within the period of 1 second for T_{in} = 60 °C. Whereas for T_{in} = 30 °C the clogging of the 2nd microchannel along with annular flow pattern is noticed 4 times within the same period of 1 second. It is found due to almost doubled wall superheat at the inception of Type 1 interaction for T_{in} = 30 °C (ΔT_{sup} ~ 5 °C) compared to T_{in} = 60 °C (ΔT_{sup} ~ 2.5 °C). Unlike the single-phase flow of T_{in} = 30 °C, a stable, weak, bubbly flow is observed in the central microchannel for T_{in} = 60 °C. Furthermore, by comparing the flow patterns in central channels for T_{in} = 30 and 60 °C (after ONB$_{cen}$), it is found that for T_{in} = 60 °C the number of nucleating bubbles increases and their sizes are larger. At higher subcooling the size of bubbles in central channels remains very small due to the strong condensation process occurring on the interface of the nucleating bubbles; the condensation effect reduces with the increase in T_{in}. Hence, it can be concluded that the effect of asymmetric fluid flow distribution on the non-uniformity of flow boiling between parallel MCHS microchannels reduces with the increase of the subcooled liquid inlet temperature. Also, on the inception of flow boiling at the lowest mass flux (G = 99 kg/m²s) strong flow reversal intensity is observed (Type 3 interaction appears directly), which leads to the condition of mirage confinement in central microchannels. The combined effect of low fluid momentum and high inlet temperature of the subcooled liquid seems to be responsible for the observed behavior. With increased mass flux the non-uniformity of flow distribution increases, Type 1 and Type 2 interactions start appearing, as explained previously.

Figure 20 shows the trend of ΔT_s for different mass fluxes at T_{in} = 60 °C. It can be observed that ΔT_s trends are fairly similar to those for T_{in} = 30 °C (Figs. 14 and 16) during flow boiling. However, lower magnitude is observed for $\Delta T_{s,cen}$ and $\Delta T_{s,side}$ at higher inlet temperature. It is primarily due to the reduced non-uniformity of temperature at the upstream location of the central and the side microchannels. Furthermore, Type 3 interaction appears at the highest mass flux (G = 392 kg/m²s) for T_{in} = 60, unlike T_{in} = 30 °C. The above observation can be accredited to the reduced subcooling effect of the incoming fluid stream. In Fig. 21, $\Delta T_{t,avg}$ is shown at T_{in} = 60 °C for different mass fluxes. Similar to $\Delta T_{s,}$ the temperature non-uniformity in the transverse direction

is reduced at higher T_{in}. It is found that $\Delta T_{t,avg}$ lies within the range of 4.3 – 9.7 ℃ for $G = 99 -$ 392 kg/m^{2}s at $T_{in} = 30$ ℃, and reduces to 2.7 – 5.3 ℃ at $T_{in} = 60$ ℃. Thus, uniform temperature distribution is maintained at higher T_{in}.

4.8 Pressure drop

Figure 22 shows pressure drop (ΔP) as a function of heat flux during flow boiling in microchannels at different mass fluxes and $T_{in} = 30$ ℃. It is noticed that ΔP experiences a sudden rise after the inception of flow boiling. This surge is found to be due to increased flow resistance caused by the additional two-phase frictional and acceleration losses during flow boiling. After the inception of flow boiling huge fluctuations in the pressure drop are observed, which are due to the generation of periodic flow reversal processes in side microchannels for all mass flow rates. This instability has been classified as pressure drop oscillation by Qu and Mudawar [21]. In Fig. 23 (a), the transient pressure drop of cases just before and after the boiling process are compared at $T_{in} = $ 30 ℃ and $G = 295$ kg/m^{2}s. It is observed that after OFR$_{side}$ the transient outlet pressure becomes higher than the inlet pressure within certain time durations, which results in a negative overall pressure drop. Due to the higher transient outlet pressure, downstream compressibility (discussed in sub-section 3.4) is observed. With the increase in heat flux, Type 2 interaction begins, that increases pressure oscillations and their magnitude. The pressure drop attains maxima at $q''_{eff} = $ 69.1 W/cm^2 for $G = 295$ kg/m^{2}s; after that a zone of nearly constant pressure drop is observed for $q''_{eff} = 69.1 - 75.1$ W/cm^2, the pressure drop starts rising again after $q''_{eff} > 75.1$ W/cm^2. The presence of the transient negative pressure drop due to the appearance of a back and forth motion of vapor in the microchannels is responsible for a slightly relaxed overall pressure drop. It is noticed that with the increase of heat flux the intensity of flow reversal increases; thus, high inlet pressure is required to maintain constant fluid supply. Moreover, high inlet pressure suppresses pressure oscillations during flow boiling; as a result, a decrease in pressure drop oscillations is noticed after attaining maxima at $q''_{eff} = 70.8$ W/cm^2 until MFR$_{cen}$.

In Fig. 23 (b), transient pressure drop in two cases: just before boiling (single-phase) and two-phase flow at the inception of Type 3 interaction, is compared. It is observed that the cyclic presence of mirage confinement near the inlet of central channels increases fluid flow resistance which leads to a rise in pressure drop as well as pressure drop oscillation. Furthermore, it can also be seen from Fig. 23 (b) that the transient pressure drop > 0, this is caused by an increase in the

upstream pressure, due to the combined effect of increased flow boiling intensity and MFR_{cen}. A fairly similar pressure drop behavior is observed for other mass fluxes. In Fig. 24 (a), transient pressure drop values at the inception of Type 1 interaction and MFR_{cen} for $G = 99$ and 295 kg/cm^{2}s are compared . It is noticed that the negative pressure drop is more severe due to low fluid flow momentum in the case of low mass flux. Furthermore, no negative transient pressure drop is observed at MFR_{cen} for $G = 295$ kg/cm^{2}s, whereas negative transient pressure drop values are found in the lower mass flux case. On increasing the heat flux further at low mass flow rate, appreciable rise in the inlet and outlet pressure as well as overall pressure drop is noticed, which causes premature CHF (Ref. Sec. 4.6) due to more significant dry out regions. Qu and Mudawar [21] also reported that severe pressure drop oscillations may result in the occurrence of premature CHF.

5.   Conclusions

The present study explores the negative influence of flow maldistribution on flow boiling in a parallel MCHS. A detailed analysis of flow boiling patterns and temperature distribution in central microchannels and side microchannels is carried out. The main findings of the current study are following:

1. It is found that boiling always incepts first in side microchannels which are poorly fed with cooling liquid in the I- type flow configuration (used in the present study) due to flow maldistribution. Periodic flow reversal up to the inlet manifold is observed in the 1st and 2nd side microchannels at ONB_{side}, whereas weak stable bubbly flow is observed in the neighboring channels. At this stage, the flow in central microchannels remains predominantly in single-phase.

2. Flow boiling intensity increases with the increase in heat flux, and more parallel microchannels (towards the center most channel) start experiencing rapid bubble growth. At high heat flux, the vapor backflow of side microchannels reaches central microchannels, leading to mirage confinement and flow reversal in those central microchannels.

27

3. Stream-wise temperature difference decreases after the inception of flow boiling for both central and side microchannels; however, this decreasing trend ceases after the appearance of mirage flow reversal in the central microchannel. It signifies that the boiling process starts approaching unstable working conditions, especially for low mass flux.

4. The average temperature of side microchannels, compared to central microchannels, is higher during single-phase as well as flow boiling. This difference increases with heat flux due to the early appearance of a partial dry-out of side channels.

5. Higher mass flux suppresses flow reversal instability in side microchannels, and the condition of mirage flow reversal in central channels is not observed even for the highest studied mass flux. However, the temperature and flow boiling non-uniformity both increase with the increase of flow rate, on account of rising flow distribution asymmetry.

6. Higher fluid inlet temperature results in uniform temperature distribution in the transverse direction; as a result, the non-uniformity of flow boiling propagation in the transverse direction reduces compared to the lower fluid inlet temperature instance.

7. The inception of flow reversal instability in side microchannels results in a sudden rise in pressure drop. With the increase of heat flux, a stable zone is observed due to weak alternating flow reversal. However, the pressure again starts to drop as mirage flow reversal instability incepts in central microchannels.

Acknowledgements

Nomenclature

A	base area of MCHS, m^2
Bd	Bond number ($g(\rho_f - \rho_g)D_h^2/\sigma$)
CHF	critical heat flux
cl	connecting line
Co	confinement number ($\sqrt{\sigma/g(\rho_f - \rho_v)D_h^2}$)
c_p	specific heat, kJ/kg/K
G	mass flux, kg/m^2/s
H	height, m
I	current, A
k	thermal conductivity of copper, W/m/K
L	length, m
M_1	deep manifold
M_2	shallow manifold

$\dot{m}$	mass flow rate, kg/s
MCHS	microchannel heat sink
N	number of microchannels
Nu	Nusselt number during single-phase flow
ΔP	pressure drop, Pa
q	heat supplied, W
q''_{eff}	effective heat flux at the base of MCHS
Re	Reynolds number ($\rho_f u D_h / \mu_f$)
t	time, s
T	temperature, ^{o}C
u	velocity, m/s
V	voltage, V
W	width, m
$z1$	distance of thermocouples tip from top of microchannels, m)

Subscript

b	tip of thermocouple
c	sudden contraction
ch	channel
cl	connecting line
e	sudden expansion

30

f	fluid
HS	heat sink
i	channel number
in	inlet
M1	deep manifold
M2	shallow manifold
out	outlet
sup	wall superheat
v	vapor
w	base of microchannel
x	transverse coordinate
y	longitudinal coordinate

Greek symbols

ρ	density, kg/m^3
μ	viscosity, Pa s
σ	surface tension, N/m^2

References

[1]   "Microprocessor Chronology" https://en.wikipedia.org/wiki/Microprocessor_chronology (Accessed 09 April, 2020)

[2]   https://www.kompulsa.com/much-power-computers-consume/ (Accessed 09 April, 2020)

[3]   I.J. Missaggia, J.N. Walpole, Z.L. Liau, R.J. Phillips, R. J., Microchannel Heat Sinks for Two-Dimensional High-Power-Density Diode Laser Arrays, IEEE J. Quantum Electron. 25 (9) (1989) 1988-1992.

[4]   J. Lee, I. Mudawar, Two-Phase Flow in High-Heat-Flux Micro-Channel Heat Sink for Refrigeration Cooling Applications: Part I-Pressure Drop Characteristics, Int. J. Heat Mass Transfer 48 (5) (2005) 928-940.

[5]   R. Nacke, B. Northcutt, I. Mudawar, Theory and Experimental Validation of Cross-Flow Micro-channel Heat Exchanger Module with Reference to High Mach Aircraft Gas Turbine Engines, Int. J. Heat Mass Transfer 54 (5-6) (2011) 1224-1235.

[6]   S. Tripathi, A. Prabhakar, N. Kumar, S.G. Singh, A. Agrawal, Blood Plasma Separation in Elevated Dimension T-Shaped Microchannel, Biomed. Microdevices 15 (3) (2013) 415-425.

[7]   R.Sh. Abiev, Y.N. Pavlyukova, O.M. Nesterova, S.D. Svetlov, V.A. Ostrovskii, Mass Transfer Intensification of 2-Methyl-5-Nitrotetrazole Synthesis in Two-Phase Liquid–Liquid Taylor Flow in Microreactor, Chem. Eng. Res. Des. 144 (2019) 444-458.

[8]   V. Yadav, R. Kumar, A. Narain, Mitigation of Flow Maldistribution in Parallel Microchannel Heat Sink, IEEE Trans. Compon. Packag. Manuf. Technol. 9 (2) (2018) 247-261.

[9]   P.A. Kew, K. Cornwell, Correlations for the Prediction of Boiling Heat Transfer in Small Diameter Channels, Appl. Therm. Eng. 17 (8-10) (1997) 705-715.

[10]   C.L. Ong, J.R. Thome, Macro-to-Microchannel Transition in Two-Phase Flow: Part 1 – Two-Phase Flow Patterns and Film Thickness Measurements, Exp. Therm. Fluid Sci. 35 (1) (2011) 37-47.

[11]   T. Harirchian, S.V. Garimella, Boiling Heat Transfer and Flow Regimes in Microchannels– A Comprehensive Understanding, J. Electron. Packag. 133 (1) (2011) 011001.

[12]   S.G. Kandlikar, Fundamental Issues Related to Flow Boiling in Minichannels and Microchannels, Exp. Therm. Fluid Sci. 26 (2-4) (2002) 389-407.

[13]   P.C. Lee, F.G. Tseng, C. Pan, Bubble Dynamics in Microchannels. Part I: Single Microchannel, Int. J. Heat Mass Transfer 47 (25) (2004) 5575-5589.

[14]   S.G. Kandlikar, Nucleation Characteristics and Stability Considerations During Flow Boiling in Microchannels, Exp. Therm. Fluid Sci. 30 (5) (2006) 441-447.

[15]   R. Revellin, J.R. Thome, A Theoretical Model for the Prediction of the Critical Heat Flux in Heated Microchannels, Int. J. Heat Mass Transfer 51 (5-6) (2008) 1216-1225.

[16]   W. Qu, S.M. Yoon, I. Mudawar, Two-Phase Flow and Heat Transfer in Rectangular Micro-Channels, ASME J. Electron. Packag. 126 (3) (2014) 288-300.

[17]   C.B. Tibirica, G. Ribatski, Flow Patterns and Bubble Departure Fundamental Characteristics during Flow Boiling in Microscale Channels, Exp. Therm. Fluid Sci. 59 (2014) 152-165.

[18]   S.T. Kadam, K. Baghel, R. Kumar, Simplified Model for Prediction of Bubble Growth at Nucleation Site in Microchannels, ASME J. Heat Transfer 136 (6) (2014) 061502.

[19]   R. Kumar, S.T. Kadam, Development of New Critical Heat Flux Correlation for Microchannel Using Energy-Based Bubble Growth Model, ASME J. Heat Transfer 138 (6) (2016) 061502.

[20]   T.A. Kingston, J.A. Weibel, S.V. Garimella, High-frequency Thermal-Fluidic Characterization of Dynamic Microchannel Flow Boiling Instabilities: Part 1 –Rapid-Bubble-Growth Instability at the Onset of Boiling, Int. J. Multiph. Flow 106 (2018) 179-188.

[21]   W. Qu, I. Mudawar, Measurement and Prediction of Pressure Drop in Two-Phase Micro-Channel Heat Sinks, Int. J. Heat Mass Transfer 46 (15) (2003) 2737-2753.

[22] M.E. Steinke, S.G. Kandlikar, An Experimental Investigation of Flow Boiling Characteristics of Water in Parallel Microchannels, ASME J. Heat Transfer 126 (4) (2004) 518-526.

[23] S.G. Kandlikar, W.K. Kuan, D.A. Willistein, J. Borrelli, Stabilization of Flow Boiling in Microchannels Using Pressure Drop Elements and Fabricated Nucleation Sites, J. Heat Transfer 128 (4) (2006) 389-396.

[24] A. Kosar, C.-J. Kuo, Y. Peles, Y., Suppression of Boiling Flow Oscillations in Parallel Microchannels by Inlet Restrictors, ASME J. Heat Transfer 128 (3) (2006) 251-260.

[25] C.-J. Kuo, Y. Peles, Y., Flow Boiling Instabilities in Microchannels and Means for Mitigation by Reentrant Cavities, ASME J. Heat Transfer 130 (7) (2008) 1-10.

[26] C.-J. Kuo, Y. Peles, Pressure Effects on Flow Boiling Instabilities in Parallel Microchannels, Int. J. Heat Mass Transfer 52 (1-2) (2009) 271-280.

[27] H.J. Lee, D.Y. Liu, S.-C. Yao, Flow Instability of Evaporative Micro-Channels, Int. J. Heat Mass Transfer 53 (9-10) (2010) 1740–1749.

[28] K. Balasubramanian, P.S. Lee, C.J. Teo, S.K. Chou, Flow Boiling Heat Transfer and Pressure Drop in Stepped Fin Microchannels, Int. J. Heat Mass Transfer 67 (2013) 234-252.

[29] M. Law, P.S. Lee, K. Balasubramanian, Experimental Investigation of Flow Boiling Heat Transfer in Novel Oblique-Finned Microchannels, Int. J. Heat Mass Transfer 76 (2014) 419–431.

[30] M. Law, P.S. Lee, A Comparative Study of Experimental Flow Boiling Heat Transfer and Pressure Characteristics in Straight- and Oblique-Finned Microchannels, Int. J. Heat Mass Transfer 85 (2015) 797–810.

[31] L. Gao, S.H. Bhavnani, Experimental Study of Augmented Flow Boiling in a Dielectric Fluid due to Backward and Forward Facing Stepped Microchannels, Int. J. Heat Mass Transfer 124 (2018) 484-490.

[32] S. Raj, A. Shukla, M. Pathak, M.K. Khan, A Novel Stepped Microchannel for Performance Enhancement in Flow Boiling, Int. J. Heat Mass Transfer 144 (2019) 118611.

[33] M.C. Lu, C.C. Wang, Effect of Inlet Location on the Performance of Parallel-Channel Cold Plate, IEEE Trans. Compon. Package. Technol. 29 (2006) 30-38.

[34]   R. Chein, J. Chen, Numerical Study of the Inlet/Outlet Arrangement Effect on Microchannel Heat Sink Performance, Int. J. Therm. Sci. 48 (2009) 1627-1638.

[35]   P. Minqiang, Z. Dehvai, T. Yong, C. Dongqing, CFD Based Study of Velocity Distribution among Multiple Parallel Microchannels, J. Comput. 4 (11) (2009) 1133-1138.

[36]   E.S. Cho, J.W. Choi, J.S. Yoon, M.S. Kim, Experimental Study on Microchannel Heat Sinks Considering Mass Flow Distribution with Non-uniform Heat Flux Conditions, Int. J. Heat Mass Transfer 53 (9-10) (2010) 2159-2168.

[37]   R.M. Kumaran, G. Kumaraguruparan, T. Sornakumar, Experimental and Numerical Studies of Header Design and Inlet/Outlet Configurations on Flow Mal-distribution in Parallel Micro-channels, Appl. Therm. Eng. 58 (2013) 205-216.

[38]   V.M Siva, A. Pattamatta, S.K. Das, Investigation on Flow Maldistribution in Parallel Microchannel Systems for Integrated Microelectronic Device Cooling, IEEE Trans. Compon. Package. Technol. 4 (3) (2014) 438-450.

[39]   G.D. Xia, J. Jiang, J. Wang, Y.L. Zhai, D.D. Ma, Effects of Different Geometric Structures on Fluid Flow and Heat Transfer Performance in Microchannel Heat Sinks, Int. J. Heat Mass Transfer 80 (2015) 439-447.

[40]   P. Dabrowski, M. Klugmann, D. Mikielewicz, Selected Studies of Flow Maldistribution in a Minichannel Plate Heat Exchanger, Arch. Thermodyn. 38 (3) (2017) 135-148.

[41]   I.A. Ghani, N.A.C. Sidik, N. Kamaruzzaman, W.J. Yahya, O. Mahian, The Effect of Manifold Zone Parameters on Hydrothermal Performance of Micro-Channel Heat Sink: A Review, Int. J. Heat Mass Transfer 109 (2017) 1143-1161.

[42]   R. Kumar, G. Singh, D. Mikielewicz, A New Approach for the Mitigating of Flow Maldistribution in Parallel Microchannel Heat Sink, ASME J. Heat Transfer 140 (7) (2018) 072401.

[43]   R. Kumar, G. Singh, D. Mikielewicz, Numerical Study on Mitigation of Flow Maldistribution in Parallel Microchannel Heat Sink: Channels Variable Width versus Variable Height Approach, ASME J. Electron. Packag. 141 (2) (2019) 021009.

[44]   P. Dabrowski, M. Klugmann, D. Mikielewicz, Channel Blockage and Flow Maldistribution during Unsteady Flow in a Model Microchannel Plate heat Exchanger, J. Appl. Fluid Mech. 12 (4) (2019) 1023–1035.

[45]   P. Dabrowski, Thermohydraulic maldistribution reduction in mini heat exchangers, Appl. Therm. Eng. 173 (5) (2020) 115271.

[46]   R. Kumar, R. Sh. Abiev, G. Ribatski, S. Abdullah, M. Vasilev, New Approach of Triumphing Temperature Nonuniformity and Heat Transfer Performance Augmentation in Micro Pin Fin Heat Sinks, J. Heat Transfer 142 (6) (2020) 062501.

[47]   X.F. Peng, B.X. Wang, Forced Convection and Flow Boiling Heat Transfer for Liquid Flowing Through Microchannels, Int. J. Heat Transfer 36, (1993) 3421-3427.

[48]   H.Y Li, F.G. Tseng, C. Pan, Bubble Dynamics in Microchannels. Part II: Two Parallel Microchannels, Int. J. Heat Mass Transfer 47 (25) (2004) 5591–5601.

[49]   Y. Lv, G. Xia, L. Cheng, D. Ma, Experimental Study on the Pressure Drop Oscillation Characteristics of the Flow Boiling Instability with FC-72 in Parallel Rectangle Microchannels, Int. Commun. Heat Mass Transfer 108 (2019) 104-289.

[50]   W. Qu, I. Mudawar, Flow Boiling Heat Transfer in Two-Phase Micro-Channel Heat Sinks––I. Experimental Investigation and Assessment of Correlation Methods, Int. J. Heat Mass Transfer 46 (15) (2003) 2755-2771.

[51]   K. Balasubramanian, M. Jagirdar, P.S. Lee, C.J. Teo, S.K. Chou, Experimental Investigation of Flow Boiling Heat Transfer and Instabilities in Straight Microchannels, Int. J. Heat Mass Transfer 66 (2013) 655-671.

[52]   R.A. Krishnan, K.R. Balasubramanian, S. Suresh, The Effect of Heating Area Orientation on Flow Boiling Performance in Microchannels Heat Sink Under Subcooled Condition, Int. J. Heat Mass Transfer 110 (2017) 276–293.

[53]   S.T. Kadam, R. Kumar, R. Abiev, Performance Augmentation of Single-Phase Heat Transfer in Open-Type Microchannel Heat Sink, J. Thermophysics Heat Transfer 33 (2) (2019) 416–424.

[54]   G. Hetsroni, A. Mosyak, Z. Segal, Nonuniform Temperature Distribution in Electronic Devices Cooled by Flow in Parallel Microchannels, IEEE Trans. Components Packag. Technol. 24 (1) (2001) 16-23.

[55]   G. Hetsroni, A. Mosyak, Z. Segal, E. Pogrebnyak, Two-Phase Flow Patterns in Parallel Micro-Channels, Int. J. Multiph. Flow 29 (3) (2003) 341-360.

[56]   G. Hetsroni, A. Mosyak, E. Pogrebnyak, Z. Segal, Explosive Boiling of Water in Parallel Micro-Channels, Int. J. Multiph. Flow 31 (4) (2005) 371-392.

[57]   G. Wang, P. Cheng, A.E. Bergles, Effects of Inlet / Outlet Configurations on Flow Boiling Instability in Parallel Microchannels, Int. J. Heat Mass Transfer 51 (9-10) (2008) 2267-2281.

[58]   D. Bogojevic, K. Sefiane, A.J. Walton, H. Lin, G. Cummins, Two-Phase Flow Instabilities in a Silicon Microchannels Heat Sink, Int. J. Heat Fluid Flow 30 (5) (2009) 854-867.

[59]   S.N. Ritchey, J.A. Weibel, S.V. Garimella, Local measurement of flow boiling heat transfer in an array of non-uniformly heated microchannels, Int. J. Heat Mass Transfer 71 (2014) 206–216.

[60]   R.D. Flynn, D.W. Fogg, J.M. Koo, C.H. Cheng, K.E. Goodson, Boiling flow in- teraction between two parallel microchannels, In: Proceedings of ASME IMECE, Chicago, Illinois, USA, (2006) 317–322 .

[61]   R.D. Flynn, C.H. Cheng, K.E. Goodson, Decoupled thermal and fluidic effects on hotspot cooling in a boiling flow microchannel heat sink," In: Proceedings of ASME InterPACK, Vancouver, British Columbia, Canada, (2007) 179–184.

[62]   T. Van Oevelen, J.A. Weibel, S.V. Garimella, The effect of lateral thermal coupling between parallel microchannels on two-phase flow distribution, Int. J. Heat Mass Transfer 124 (2018) 769–781.

[63]   T.A. Kingston, J.A. Weibel, S.V. Garimella, Ledinegg instability-induced tem- perature excursion between thermally isolated, heated parallel microchannels, Int. J. Heat Mass Transfer 132 (2019) 550–556.

[64]   M.E. Steinke, S.G. Kandlikar, Control and Effect of Dissolved Air in Water During Flow Boiling in Microchannels, Int. J. Heat Mass Transfer 47 (8-9) (2004) 1925-1935.

[65]   R.K. Shah, A.K. London, Laminar Flow Forced Convection in Ducts, Academic Press NY (1978).

[66]   S.G. Kandlikar, S. Garimella, D. Li, S. Colin, M.R. King, Heat Transfer and Fluid Flow in Minichannels and Microchannels, Elsevier Oxford United Kingdom (2006).

[67]   J.P. Holman, Experimental Methods for Engineers, seventh ed. Tata McGraw hill NY (2010).

[68]   A. Bejan, Convection Heat Transfer, fourth ed. John Wiley and Sons Hoboken NJ (2013).

[69]   J. Lee, I. Mudawar, Fluid flow and heat transfer characteristics of low temperature two-phase micro-channel heat sinks – Part 2. Subcooled boiling pressure drop and heat transfer,

Int. J. Heat Mass Transfer 51 (17-18) (2008) 4327–4341.

[70]   W.K. Kays, M.E. Crawford, Convective Heat and Mass Transfer, second ed. McGraw-Hill New York (1980) 275–280.

[71]   W. Tong, A.E. Bergles, M.K. Jensen, Pressure drop with highly subcooled flow boiling in small-diameter tubes, Exp. Therm. Fluid Sci. 15 (3) (1997) 202–212.

[72]   R. Kumar, V. Yadav, R.Sh. Abiev, Concurrent Removal of Heat Transfer and Mass Flow Rate Nonuniformities in Parallel Channels of Microchannel Heat Sink, Theor. Found. Chem. Eng. 54 (1) (2020) 77-90.

[73]   J. Lee, I. Mudawar, Fluid flow and heat transfer characteristics of low temperature two-phase micro-channel heat sinks – Part 1: Experimental methods and flow visualization results, Int. J. Heat Mass Transfer 51 (17-18) (2008) 4315–4326.

List of Tables

Table 1 Dimensions (mm) of microchannels

Table 2 Uncertainty in the derived parameters

List of Figures

Fig. 1 Schematic diagram of the experimental setup.

Fig. 2 Photograph of the experimental setup.

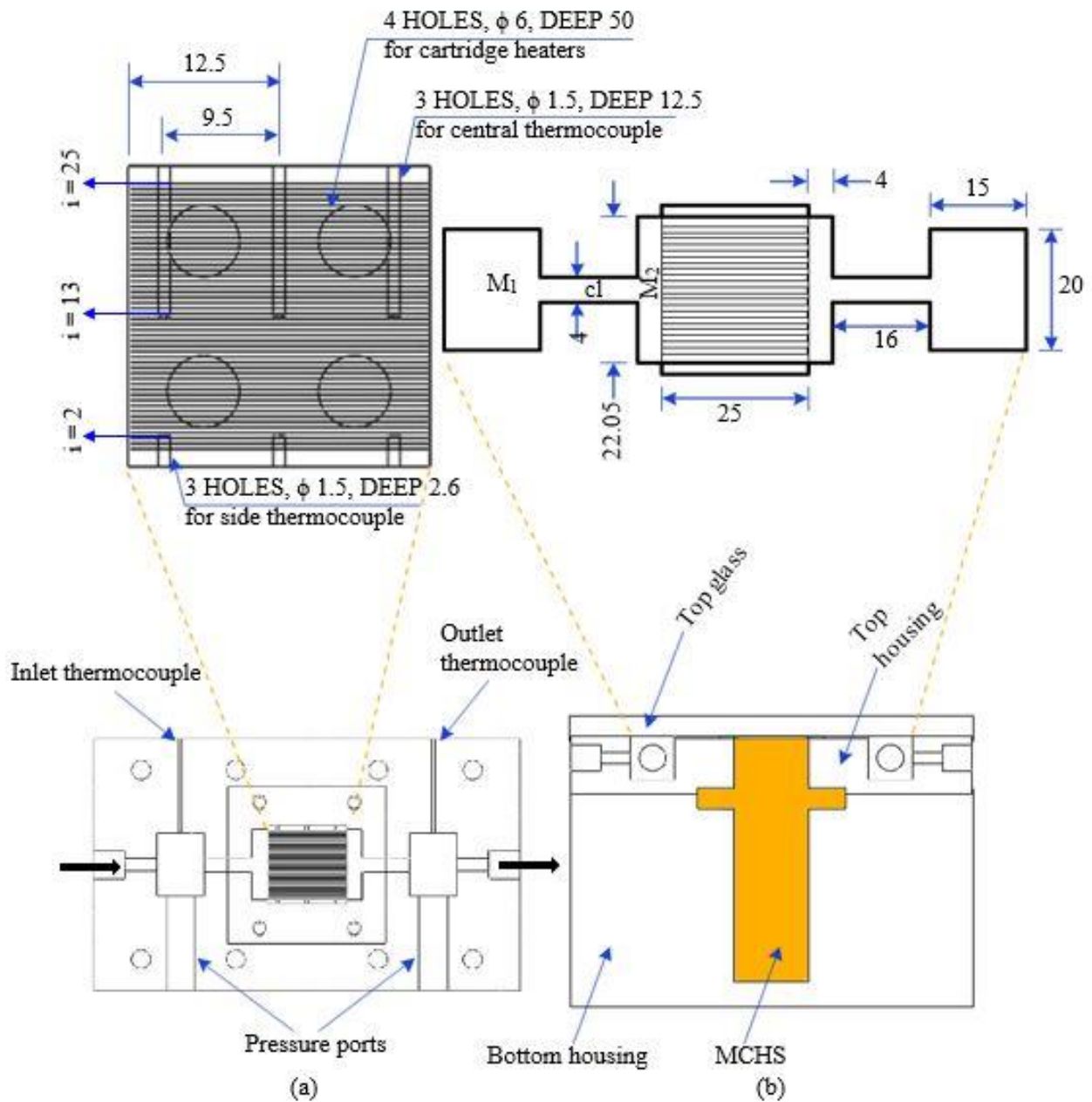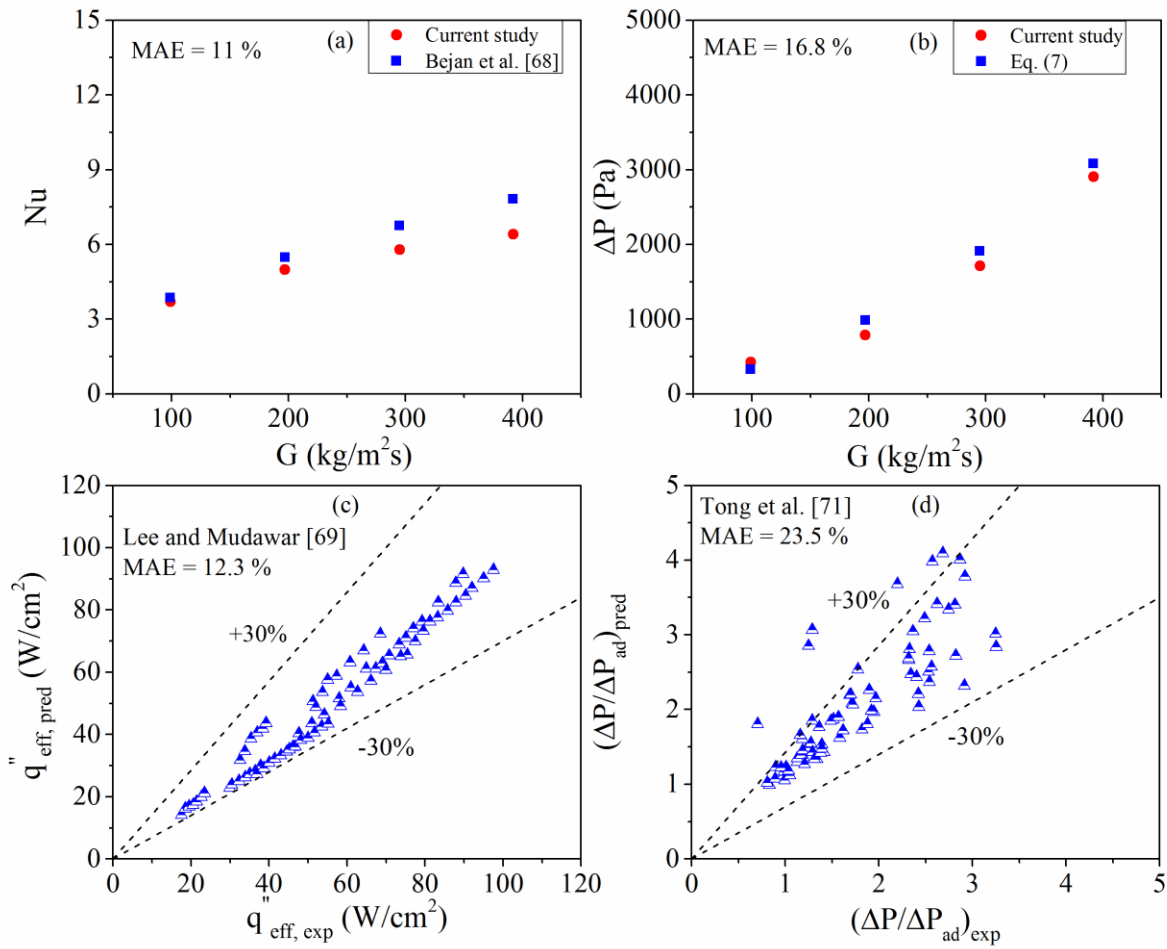**Fig. 3** Schematic of test section (a) top view (b) sectional side view (All the dimensions are in mm).

Fig. 4 Validation of current experimental results (a) single phase Nusselt number, (b) single phase pressure drop, (c) subcooled boiling heat transfer and (d) subcooled boiling pressure drop.
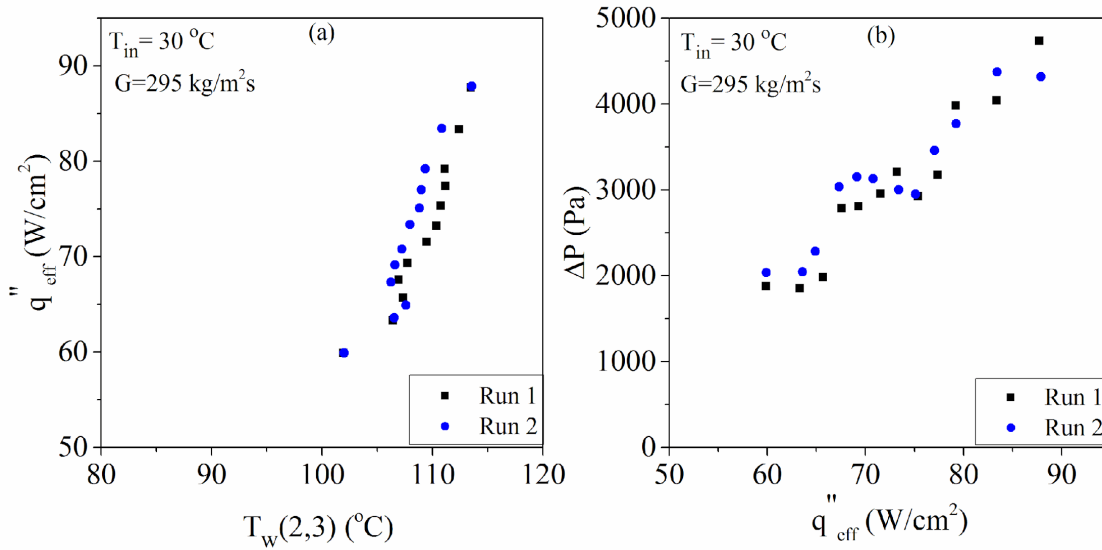
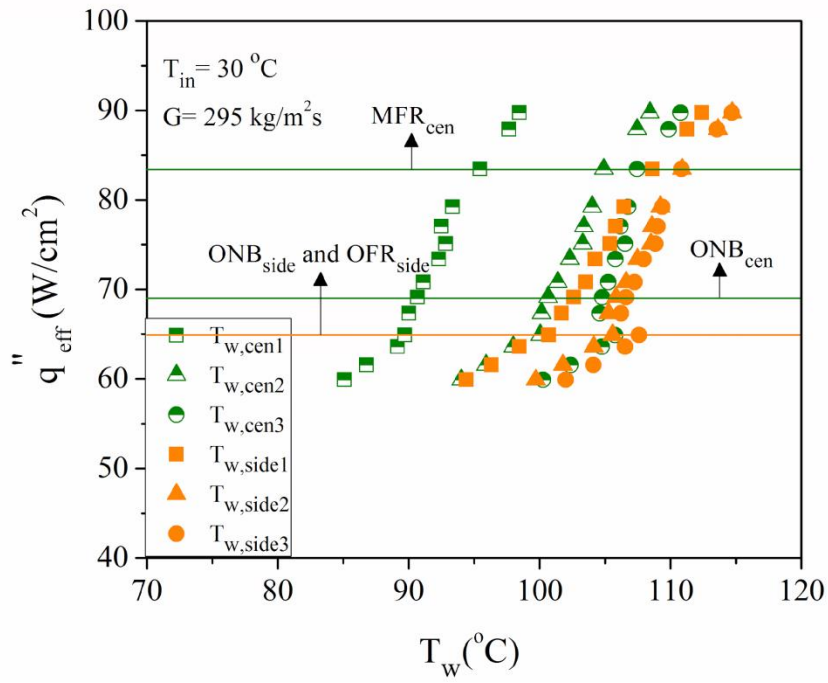**Fig. 5** Repeatability test of boiling curve and pressure drop for G = 295 kg/m^{2}s and T_{in} = 30 ^{o}C.

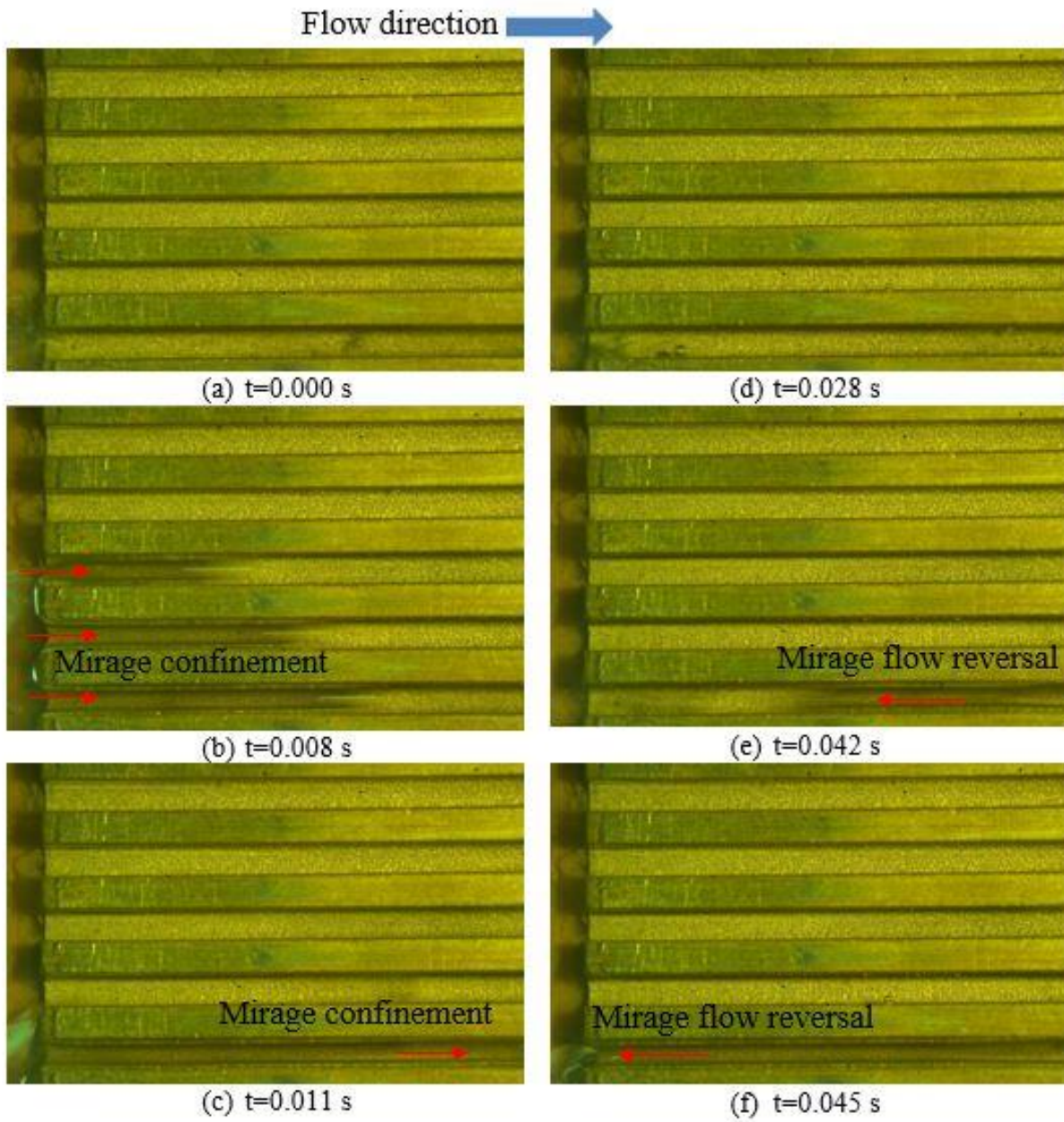**Fig. 6** Boiling curve at $G = 295$ Kg/m^{2}s and $T_{in} = 30$ ℃.

Fig. 7 Presence mirage confinement and mirage flow reversal near the inlet of central microchannels at $G = 295$ kg/m^{2}s and $q''_{eff} = 83.4$ W/cm^2.

Fig. 8 Flow pattern near the outlet of 2nd microchannel at $G = 295$ kg/m^{2}s and $q''_{eff} = 64.9$ W/cm^2.

Fig. 9 Interaction of entrapped vapor near the outlet of $1 - 4$ microchannels with fluid of outlet manifold at $G = 295$ kg/m^{2}s and $q''_{eff} = 69.1$ W/cm^2.

Fig. 10 Flow pattern near the outlet of 3rd microchannel at $G = 295$ kg/m^{2}s and $T_{in} = 30$ ℃ (a) q''_{eff} = 67.3 W/cm^2 and (b) $q''_{eff} = 73.4$ W/cm^2.

Fig. 11 Effect of flow reversal in side microchannels ($i = 1 - 2$) on flow patterns in neighboring microchannels ($i = 3 - 5$) at $G = 295$ kg/m^{2}s and $q''_{eff} = 67.3$ W/cm^2.

Fig. 12 Flow patterns interactions (Type 2) near the inlet of side microchannels ($i = 1 - 4$ from bottom to top) at $G = 295$ kg/m^{2}s and $q''_{eff} = 67.3$ W/cm^2.

Fig. 13 Flow regimes near the inlet of outlet of 5 central ($i = 11 - 15$ from bottom to top) and 5 side microchannels ($i = 1 - 5$ from bottom to top) at $G = 295$ kg/m^{2}s and (a) $q''_{eff} = 79.2$ W/cm^2 and (b) $q''_{eff} = 83.4$ W/cm^2.

Fig. 14 Temperature difference in the (a) streamwise and (b) transverse direction at $G = 295$ kg/m^{2}s and $T_{in} = 30$ ºC.

Fig. 15 Boiling curve at different mass fluxes and $T_{in} = 30$ ºC.

Fig. 16 Effect of heat flux on temperature difference during flow boiling at $T_{in} = 30$ ºC (a) temperature difference in the streamwise direction (ΔT_s) and (b) average temperature difference in transverse direction ($\Delta T_{t,avg}$) at different mass fluxes.

Fig. 17 Flow regimes near the inlet and outlet of 5 central ($i = 11 - 15$ from bottom to top) and 5 side microchannels ($i = 1 - 5$ from bottom to top) at $q''_{eff} = 83.4$ W/cm^2 for (a) $G = 295$ kg/m^{2}s and (b) $G = 392$ kg/m^{2}s.

Fig. 18 Boiling curves at different mass fluxes and $T_{in} = 60$ ºC.

Fig. 19 Comparison of flow regimes of (a) 5 central and (b) 5 side microchannels at ONB$_{side}$ for $T_{in} = 30$ ºC and $T_{in} = 60$ ºC at $G = 295$ kg/m^{2}s.

Fig. 20 Effect of heat flux on streamwise temperature difference at different mass fluxes and $T_{in} = 60$ ºC.

Fig. 21 Effect of heat flux on average transverse temperature difference at different mass fluxes and $T_{in} = 60$ ºC.

Fig. 22 Pressure drop (ΔP) at different mass fluxes.

Fig. 23 Oscillations in pressure drop at $G = 295$ kg/cm^{2}s and different heat fluxes.

Fig. 24 Oscillations in pressure drop for $G = 99$ and 295 kg/m^{2}s and at (a) Type 1 and (b) MFR$_{cen}$.

Table 1 Dimensions (mm) of microchannls

W_{ch}	W_{fin}	H_{ch}	L_{ch}	W_{sw}
0.45	0.45	0.725	25	1.475

Table 2 Uncertainty in the derived parameters

Parameter	Uncertainty
D_h	3 μm
G	4.4-17.5 %
q''_{eff}	2.6-3.4 %
Nu	3.2-6.4 %

P – Pressure transducers

T – Thermocouple

DAS – Data acquisition system
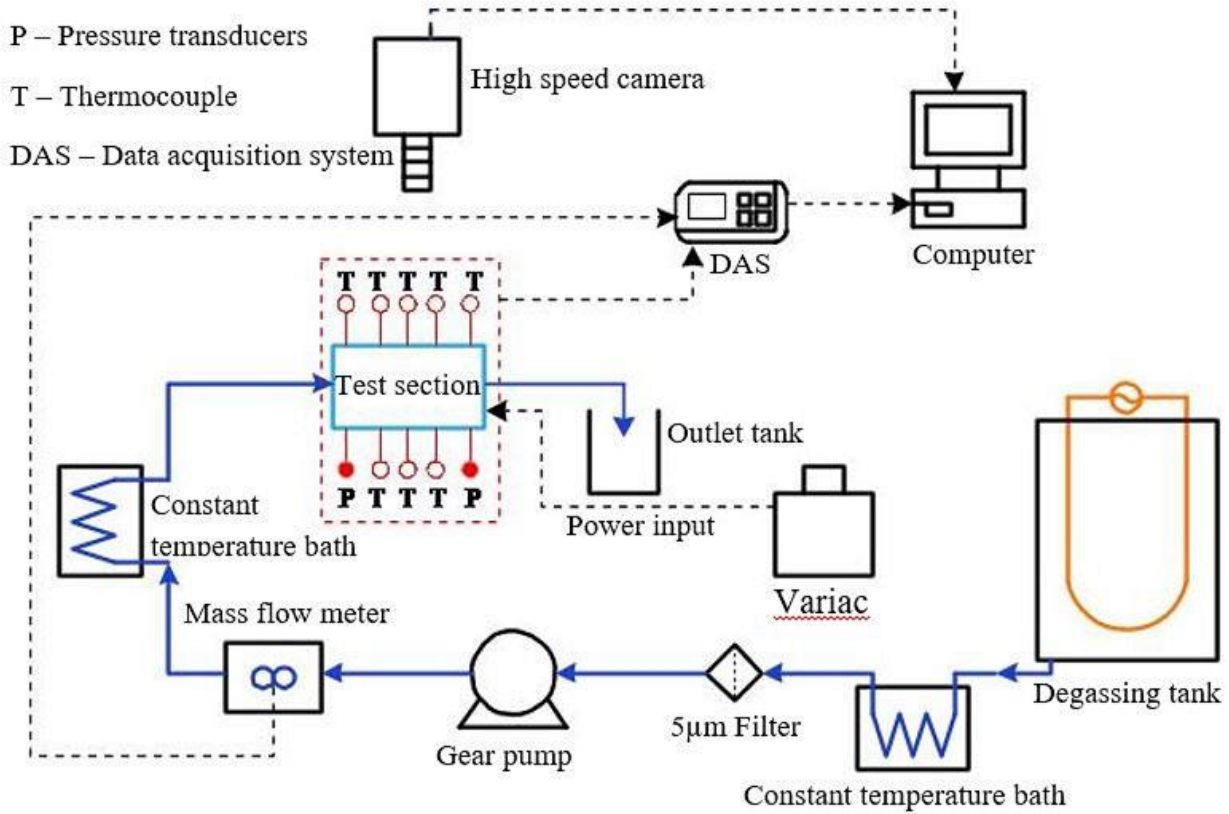
Fig. 1 Schematic diagram of the experimental setup.

1 Degassing tank	5 Test section	9 Autotransformer
2 Gear pump	6 High speed camera	10 Data acquisition system
3 Mass flow meter	7 Laser light source	11 Wattmeter
4 Constant temperature bath	8 3-axis movement slider	12 Personal computer

Fig. 2 Photograph of the experimental setup.

Fig. 3 Schematic of test section (a) top view (b) sectional side view (All the dimensions are in mm).

44

Fig. 4 Validation of current experimental results (a) single phase Nusselt number, (b) single phase pressure drop, (c) subcooled boiling heat transfer and (d) subcooled boiling pressure drop.

Fig. 5 Repeatability test of boiling curve and pressure drop for G = 295 kg/m^{2}s and T_{in} = 30 ^{o}C.

Fig. 6 Boiling curve at $G = 295$ kg/m^{2}s and $T_{in} = 30$ ^{o}C.

Flow direction ➡

(a) t=0.000 s

(d) t=0.028 s

Mirage confinement

(b) t=0.008 s

Mirage flow reversal

(e) t=0.042 s

Mirage confinement

(c) t=0.011 s

Mirage flow reversal

(f) t=0.045 s

Fig. 7 Presence mirage confinement and mirage flow reversal near the inlet of central microchannels at $G = 295$ kg/m^{2}s and $q''_{eff} = 83.4$ W/cm^2.

Fig. 8 Flow pattern near the outlet of 2nd microchannel at $G = 295$ kg/m^{2}s and $q''_{eff} = 64.9$ W/cm^2.

Fig. 9 Interaction of entrapped vapor near the outlet of 1 – 4 microchannels with fluid of outlet manifold at $G = 295$ kg/m^{2}s and $q''_{eff} = 69.1$ W/cm^2.

Fig. 10 Flow pattern near the outlet of 3rd microchannel at G = 295 kg/m^{2}s and T_{in} = 30 ^{o}C (a) q''_{eff} = 67.3 W/cm^2 and (b) q''_{eff} = 73.4 W/cm^2.

Fig. 11 Effect of flow reversal in side microchannels ($i = 1 - 2$) on flow patterns in neighboring microchannels ($i = 3 - 5$) at G = 295 kg/m²s and q''_{eff} = 67.3 W/cm².

Fig. 12 Flow patterns interactions (Type 2) near the inlet of side microchannels ($i = 1 - 4$ from bottom to top) at $G = 295$ kg/m²s and $q''_{eff} = 67.3$ W/cm².

Fig. 13 Flow regimes near the inlet of outlet of 5 central (i = 11 – 15 from bottom to top) and 5 side microchannels (i = 1 – 5 from bottom to top) at G = 295 kg/m²s and (a) q''_{eff} = 79.2 W/cm² and (b) q''_{eff} = 83.4 W/cm².

Fig. 14 Temperature difference in the (a) streamwise and (b) transverse direction at $G = 295$ kg/m²s and $T_{in} = 30$ °C.

Fig. 15 Boiling curve at different mass fluxes and $T_{in} = 30$ °C.
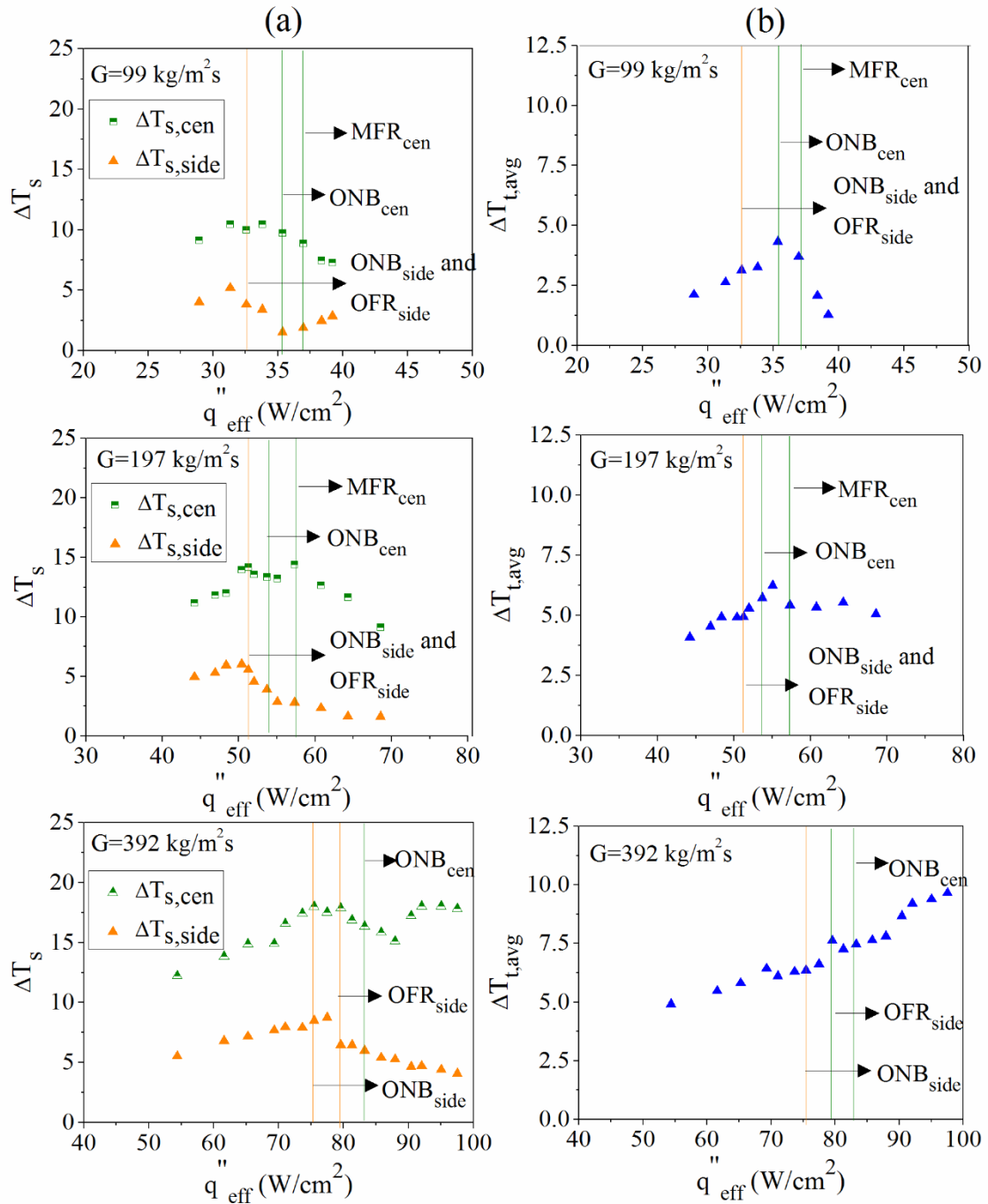
Fig. 16 Effect of heat flux on temperature difference during flow boiling at $T_{in} = 30\ ^oC$ (a) temperature difference in the streamwise direction (ΔT_s) and (b) average temperature difference in transverse direction ($\Delta T_{t,avg}$) at different mass fluxes.
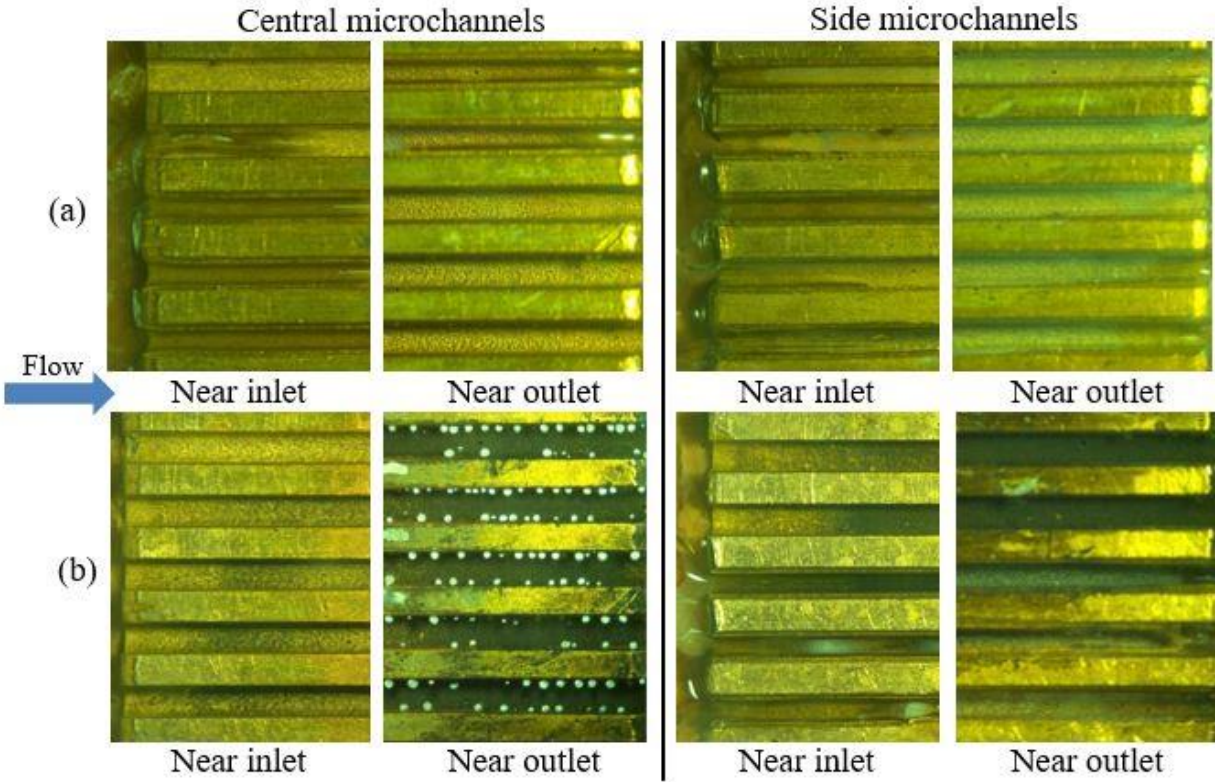
Fig. 17 Flow regimes near the inlet and outlet of 5 central ($i = 11 - 15$ from bottom to top) and 5 side microchannels ($i = 1 - 5$ from bottom to top) at $q''_{eff} = 83.4$ W/cm^2 for (a) $G = 295$ kg/m^{2}s and (b) $G = 392$ kg/m^{2}s.
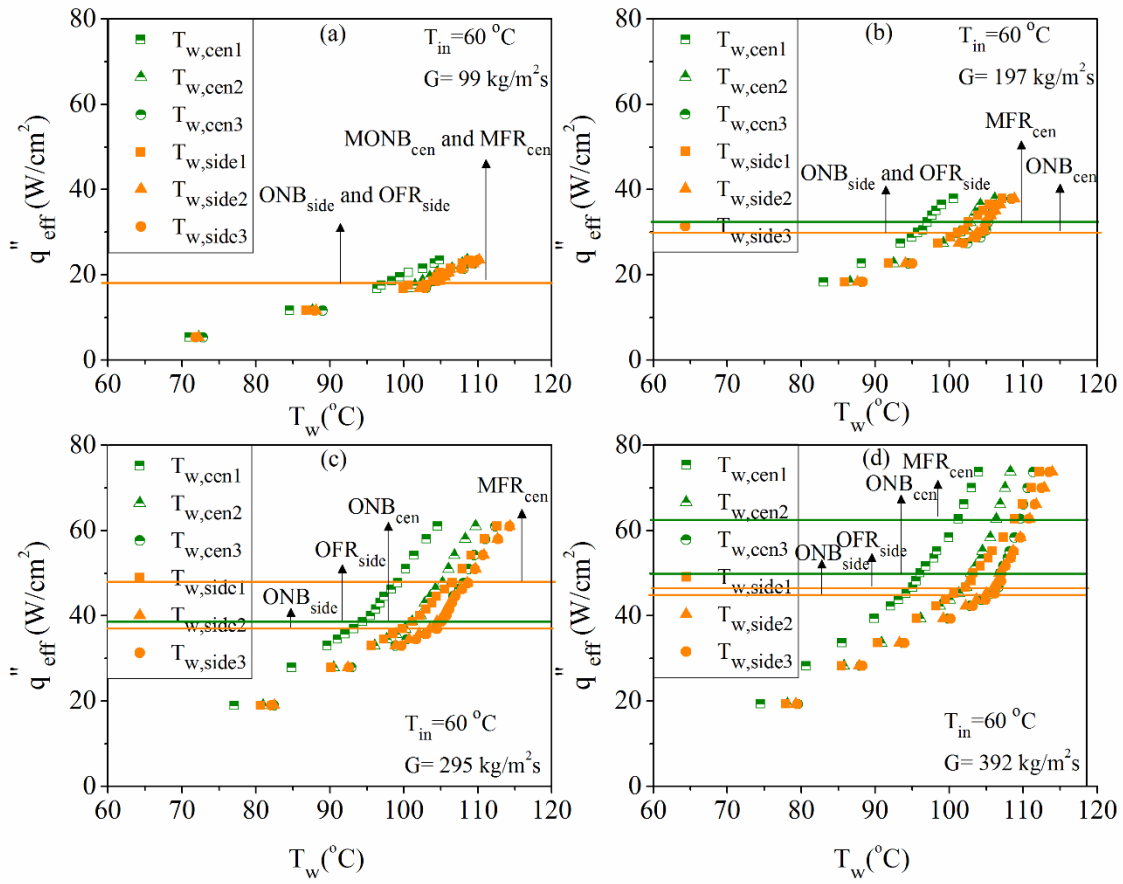
Fig. 18 Boiling curves at different mass fluxes and T_{in} = 60 °C.

Fig. 19 Comparison of flow regimes of (a) 5 central and (b) 5 side microchannels at ONB$_{side}$ for $T_{in} = 30$ ^{o}C and $T_{in} = 60$ ^{o}C at $G = 295$ kg/m^{2}s.
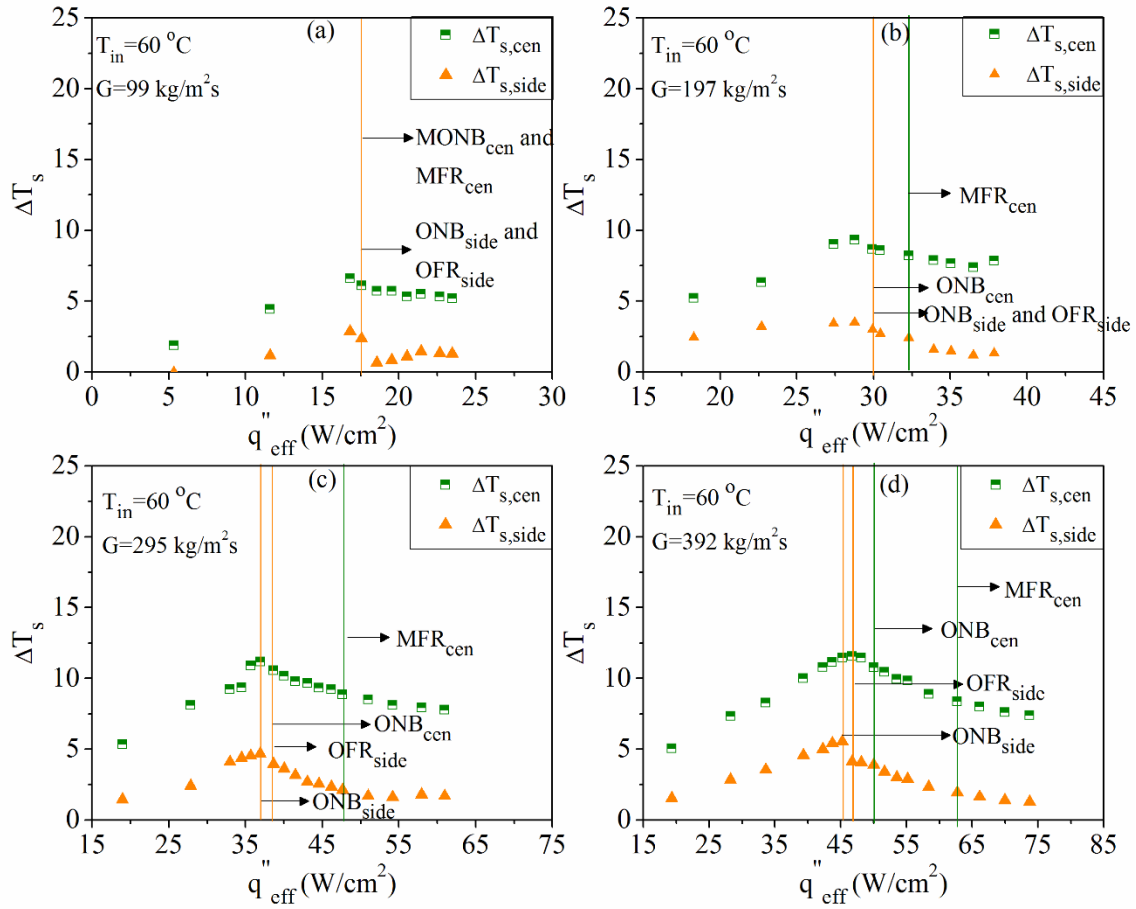
Fig. 20 Effect of heat flux on streamwise temperature difference at different mass fluxes and T_{in} = 60 °C.

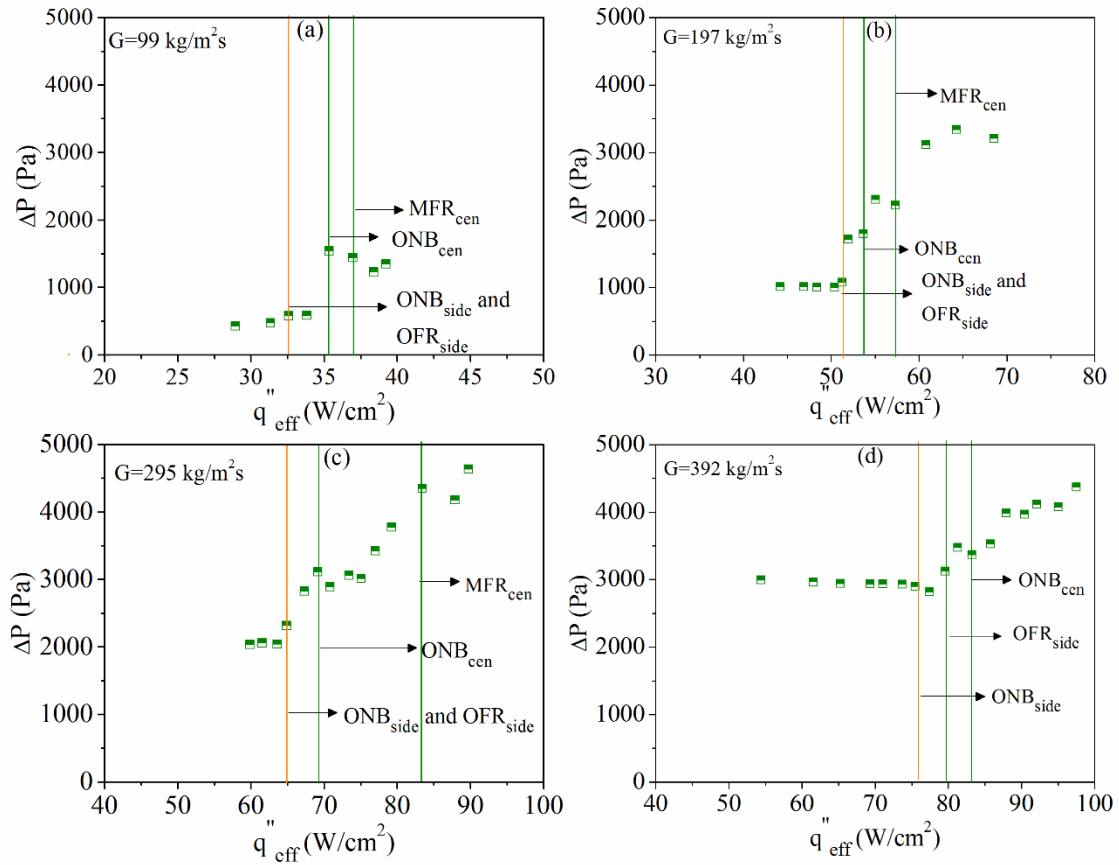**Fig. 21** Effect of heat flux on average transverse temperature difference at different mass fluxes and $T_{in} = 60$ ℃.
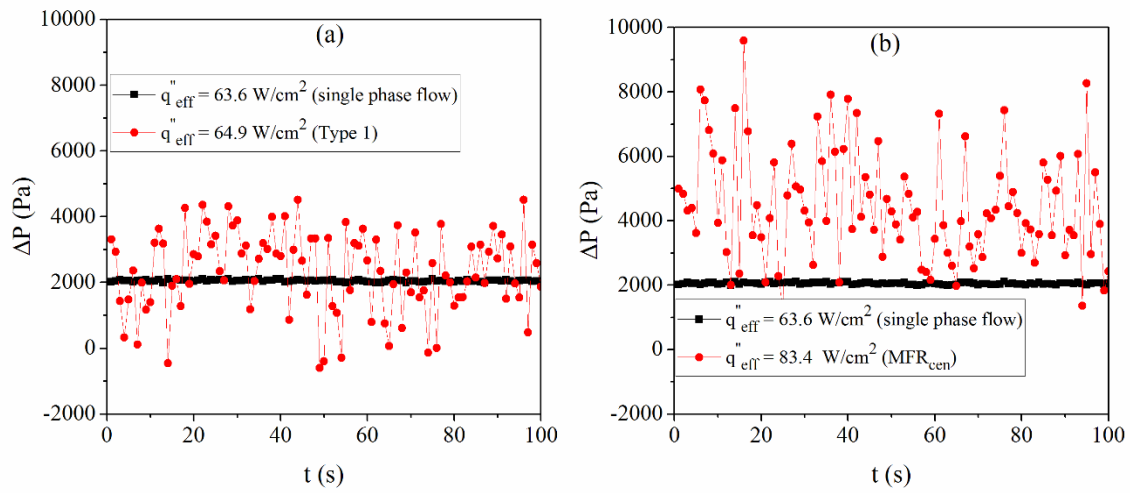
Fig. 22 Pressure drop (*ΔP*) at different mass fluxes.

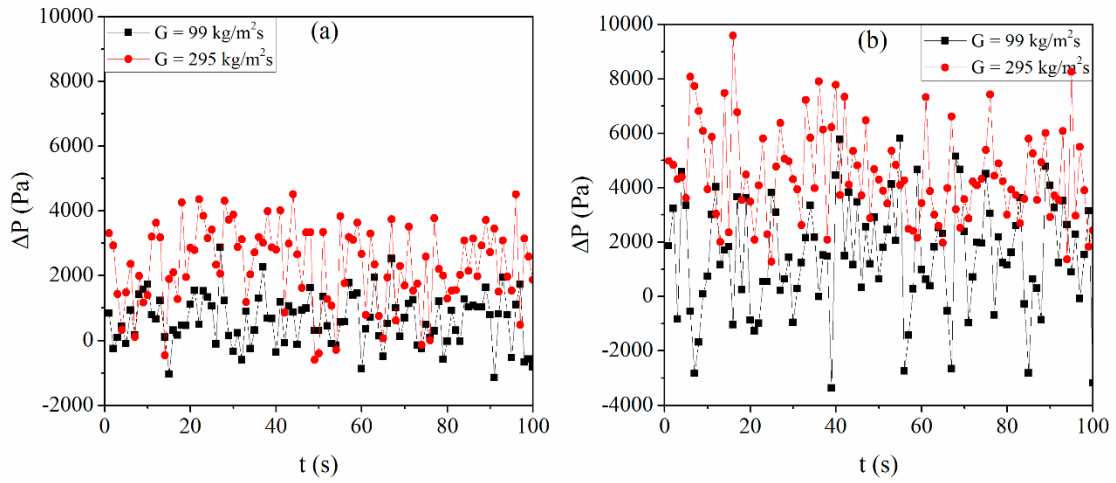**Fig. 23** Oscillations in pressure drop at G = 295 kg/cm^{2}s and different heat fluxes.

Fig. 24 Oscillations in pressure drop for G = 99 and 295 kg/m^{2}s and at (a) Type 1 and (b) MFR$_{cen}$.